

G³Splat: Geometrically Consistent Generalizable Gaussian Splatting

Mehdi Hosseinzadeh^{1,*†} Shin-Fang Chng^{2*} Yi Xu² Simon Lucey¹ Ian Reid^{1,3} Ravi Garg¹

¹ Australian Institute for Machine Learning ² Goertek Alpha Labs ³ MBZUAI

m80hz.github.io/g3splat

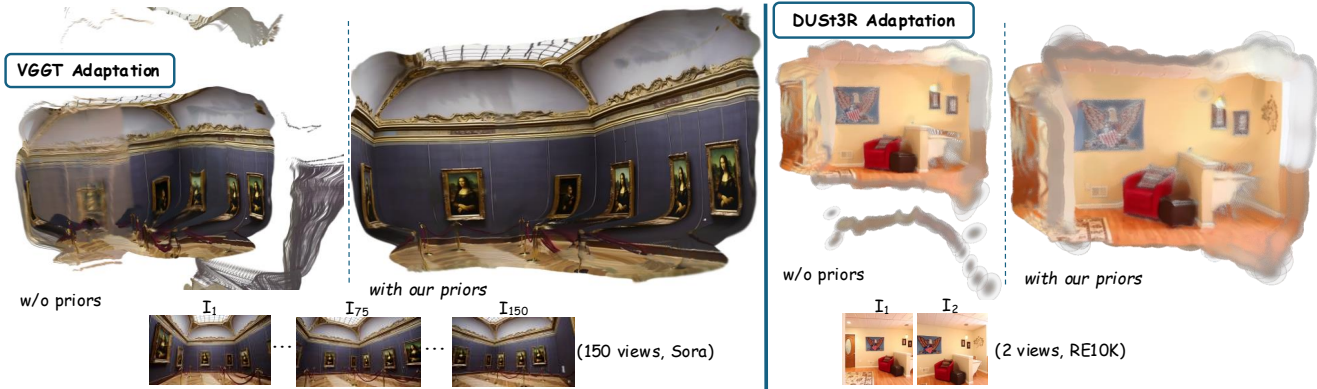


Figure 1. **G³Splat enables geometrically consistent, pose-free generalizable Gaussian splatting across backbones.** **Left:** our VGQT-based [56] adaptation *without* / *with* the proposed priors. **Right:** our DUST3R-based [58] adaptation *without* / *with* the proposed priors. We visualize reconstructions on a Sora-generated video (150 input views) and RealEstate10K [75] (2 input views). Our priors encourage *geometrically consistent* Gaussians and markedly reduce floating artifacts. Sora prompt: “Generate a video inside the Louvre Museum, including the paintings.”

Abstract

3D Gaussians have recently emerged as an effective scene representation for real-time splatting and accurate novel-view synthesis, motivating several works to adapt multi-view structure prediction networks to regress per-pixel 3D Gaussians from images. However, most prior work extends these networks to predict additional Gaussian parameters—orientation, scale, opacity, and appearance—while relying almost exclusively on view-synthesis supervision. We show that a view-synthesis loss alone is insufficient to recover geometrically meaningful splats in this setting. We analyze and address the ambiguities of learning 3D Gaussian splats under self-supervision for pose-free generalizable splatting, and introduce G³Splat, which enforces geometric priors to obtain geometrically consistent 3D scene representations. Trained on RE10K, our approach achieves state-of-the-art performance in (i) geometrically consistent reconstruction, (ii) relative pose estimation, and (iii) novel-view synthesis. We further demonstrate strong zero-shot generalization on ScanNet, substantially outperforming prior work in both geometry recovery and relative pose estimation. Code and pretrained models are released on our project page.

1. Introduction

3D Gaussian splatting (3DGS) [31] has recently revolutionized 3D structure and appearance modeling from multi-view images. Departing from traditional depth or point cloud representations of the scene structure, 3D Gaussians implicitly model surface reflections and environment lighting to encode view-dependent scene appearance. They are memory-efficient compared to explicit volumetric alternatives and facilitate rendering of the scene from arbitrary viewpoints in a fraction of a second. Due to these capabilities, 3D Gaussians have become a prevalent choice for scene representation.

Generalizable Gaussian splatting extends 3DGS from per-scene optimization to feedforward reconstruction of novel views. Instead of fitting Gaussians separately for each scene, recent methods train neural networks that predict 3D Gaussians directly from one or a few input images [3, 5, 28, 29, 48, 51, 59, 63, 68, 72]. Given these sparse views, the feedforward networks output a set of Gaussians (means, orientations, scales, and colors), achieving photorealistic novel-view synthesis.

Most existing generalizable splatting frameworks are built by adapting well-established geometry networks originally designed for dense depth [56, 62] or pixelwise 3D point prediction [35, 58]. These networks typically use image encoders to process one or multiple images, fol-

*Equal contribution. †Corresponding author.

lowed by decoders to predict Gaussian means as per-pixel depthmaps [62] or 3D points in a canonical frame [35, 56, 58] for each frame. Additional decoders are appended to the geometry predictors to predict Gaussian properties such as orientation, scale, opacity and view-dependent color – typically without much foresight. These networks are usually trained predominantly by minimizing view-synthesis loss on a few target views, closely following existing self-supervised depth estimators, but with a different image-formation mechanism due to the underlying change in scene representation. However, this prevalent setup overlooks several key issues inherited from the underlying 3DGS optimization:

- **Overparameterization:** 3D Gaussians are overparameterized compared to depth maps or point clouds. Successful estimation of 3D Gaussians typically requires a large number of densely sampled viewpoints. Few-shot 3DGS is known to require priors [7, 77] even in optimization-based settings; yet generalizable methods typically inherit the 3DGS parameterization without introducing corresponding geometry constraints during training.
- **Geometric ambiguity:** Unlike per-pixel depths or 3D point locations – which are uniquely defined (up to scale) – multiple 3D Gaussian configurations can produce equally valid renderings. This ambiguity means that purely image-based loss can let the network converge to geometrically incorrect solutions that still explain the views.
- **Lack of heuristic:** Successful per-scene Gaussian splatting methods typically rely on non-differentiable heuristics (*i.e.*, splitting, duplication and pruning of Gaussians). However, existing generalizable methods are trained purely via view-synthesis gradient loss and neglect these heuristics; *i.e.* all Gaussians remain perpetually alive throughout training.

As a result, existing generalizable Gaussian splatting methods often converge to *geometrically degenerate Gaussians*: while the predicted locations (means) remain reasonably accurate — benefiting from well-established depth or pointcloud estimators — orientations, scales, and opacities are often incorrect. As shown in Figure 2, existing generalizable splatting approaches struggle to learn meaningful opacities, orientations, or scales when trained with view-synthesis loss alone: Gaussian orientations (shown as normal maps) are misaligned with the underlying surface, and 3D Gaussians become unjustifiably elongated or collapsed (shown in scales). We observe these degeneracies both in splat predictors that anchor Gaussian centers via depth maps [5] and in those that use per-pixel 3D point maps aligned to a common reference frame [68]. Although we highlight these two representative approaches in Figure 2, similar issues appear across *all* existing generalizable splatting methods. We attribute these geometry artifacts to the inherent overparameterization of 3D splats combined with purely photometric supervision: without additional structural priors, self-supervised learning

of Gaussian parameter is ill-posed.

In this work, we aim to systematically characterize what constitutes a geometrically consistent Gaussian in the generalizable setting and propose priors that encourage such configurations. We build on a DUS3R-style [58] backbone that predicts per-pixel 3D points for pairs of input images defined in a single canonical frame. On top of this backbone, we explore both standard 3DGS [31] and "surfel-like" 2DGS representations, and study how our regularization strategies improve the geometric quality of generalizable splatting. Our main findings are:

- Aligning Gaussian's orientations with dominant local surface normals is crucial for resolving structural ambiguities. This constraint provides the essential supervision for orientation that existing frameworks currently lack.
- Standard depth-normal consistency losses [4, 26] used to enforce this constraint are not straightforward to deploy when learning splat predictors, see supplementary material for details. Instead, directly enforcing consistency between Gaussian orientations and their means by leveraging the local image neighborhood of pixel-aligned 3D Gaussians promotes stable training.
- Ensuring that predicted Gaussians are pixel-aligned is essential for self-supervision. In particular, for methods that predicts point cloud, violating pixel alignment leads to structure-pose ambiguity.
- Splat prediction frameworks can be trained with both full-rank 3D Gaussians and rank-deficient "surfel-like" Gaussians. While the added flexibility of full-rank Gaussians benefits accurate pose and structure estimation, when proposed priors are applied. These differences start to diminish when the proposed priors are applied.

Our method outperforms prior work in novel-view synthesis and, crucially, produces plausible scene geometry that enables direct depth rendering from arbitrary viewpoints – something existing generalizable methods cannot achieve. These consistent virtual depths can be fused using a Truncated Signed Distance Function (TSDF) [73]; and the reconstructed meshes provide geometric comparison against prior art, as shown in Figure 4. Beyond view synthesis, our approach establishes *state-of-the-art* relative pose estimation from image pairs, surpassing task-specific methods such as RoMa [11], geometry-supervised approaches such as DUS3R [35, 58], and pose-free generalizable splatting method [68] – despite using less data and weaker supervision in some cases. Our method achieves state-of-the-art zero-shot 3D reconstruction on ScanNet [9], outperforming both pose-free and pose-required generalizable splatting methods.

Note that we choose DUS3R [58] as the geometric backbone due to its relative simplicity (compared to [56]), and its capability to infer 3D structure without requiring relative pose between input images (unlike epipolar attention [3] or

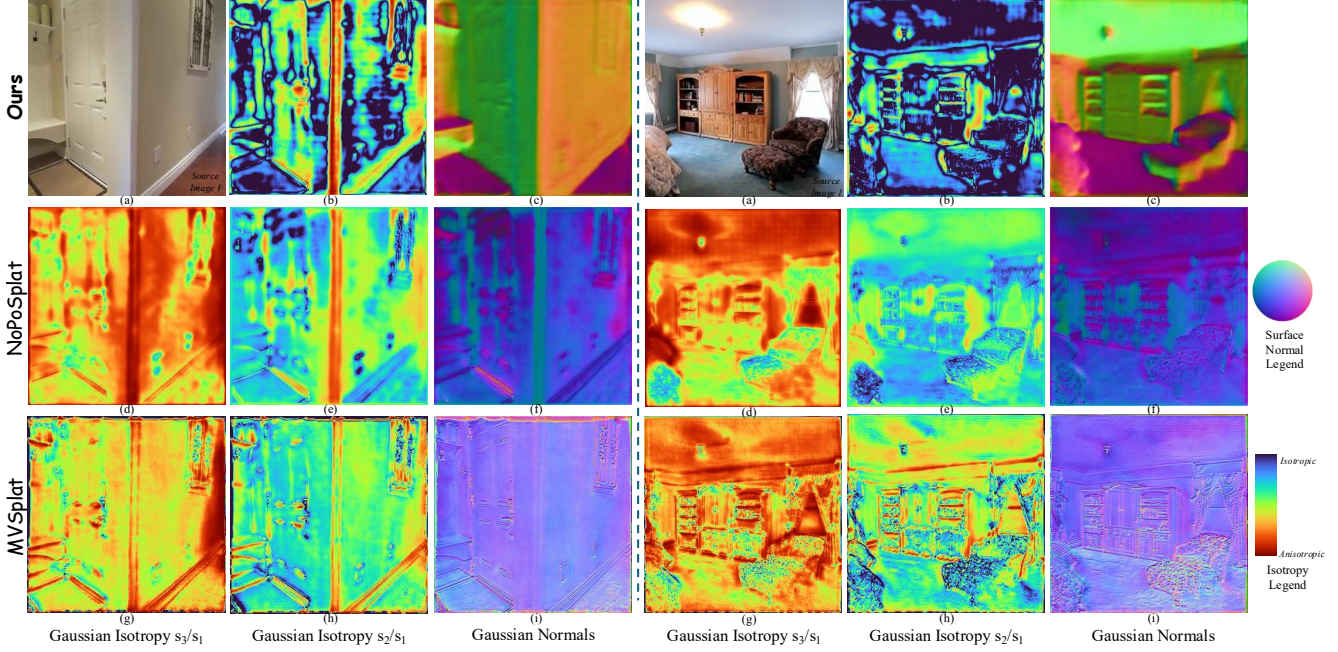


Figure 2. Qualitative comparison of predicted Gaussian parameters. For visualization, we denote by (s_1, s_2, s_3) the *sorted* eigen-scales of each Gaussian covariance in Equation (7), such that $s_1 \geq s_2 \geq s_3$; the smallest scale s_3 characterizes uncertainty along the surface normal direction. **Row 1 (ours)** shows: (a) the source image to which Gaussians are aligned, (b) skewness of the estimated Gaussians within their defining plane, and (c) predicted Gaussian orientations visualized as surface-normal maps. **Rows 2 and 3** show results for NoPoSplat [68] and MVSplat [5], respectively: (d/g) Gaussians’ elongation perpendicular to the dominant plane defined by it, (e/h) Gaussians’ skewness within the dominant plane, and (f/i) normals to the dominant plane. Existing methods yield Gaussian orientations without clear geometric meaning: MVSplat Gaussians (i) align mostly fronto-parallel to the source image plane, and NoPoSplat Gaussians orientations (f) strongly depend on texture, spanning a few dominant directions inconsistent with scene geometry. Our method produces plausible, near-Manhattan structured surface orientations. Baseline Gaussians exhibit significant elongation perpendicular to their dominant surfaces (visible as non-red colors in d/g). Notably, our Gaussians remain relatively circular (blue color in b) on planar, textureless surfaces and become skewed ellipses (red color in b) near sharp geometric edges such as shelves or wall corners.

cost-volume-based architectures [5]). However, our contributions are not tied to a specific backbone. To our knowledge, this is the *first* work in generalizable Gaussian splatting that systematically analyze and address the degeneracies in the predicted Gaussian orientation and scale, which outperforms the prior arts on various geometric measures. The proposed regularizers can be seamlessly integrated into any other geometric estimator – such as VGGT [56] – to construct corresponding splatting frameworks; in Sec. 4.2 we demonstrate the benefit of *splatting* VGGT using our priors. We believe that the presented contributions lay the groundwork for future research on training neural networks to predict Gaussians from images, in both depth- and self-supervised setups.

2. Related Work

Owing to the state-of-the-art real-time view synthesis performance of 3D Gaussian splitting [31], significant effort has been put into improving 3DGS for scenarios such as few-view reconstruction [7, 24, 36, 54, 61, 77], dynamically

moving objects [39, 60, 65, 66], surface extraction [22, 26], and incorporating object semantics into 3D reconstructions [37]. Real-time simultaneous localization and mapping approaches have also adapted Gaussian splats as an inherent scene representation [30, 41]. Additionally, Gaussian splats have been used for generating geometrically consistent images and video sequences [57, 60].

The deep learning revolution of the last decade has significantly influenced geometric inference from one or more images. Earlier works focused on training neural networks to map a single image to depth map obtained from range sensors [13, 14, 33, 34, 45]. Multi-view extensions for these supervised learning algorithms are well explored as well [2, 21, 27, 53, 55, 67]. More recently, methods have explored reconstructing registered sets of per-pixel point clouds from multiple images, providing state-of-the-art relative pose and scene structure [35, 58].

Additionally, it has been demonstrated that these feed-forward geometry predictors can be trained without depth sensors in a self-supervised manner by minimizing view

synthesis losses [16, 18, 19, 71, 74]. Structure prediction from single or few images has also been utilized as an optimization-free building block in high-fidelity tracking and mapping systems [76, 78]. Generalizable Gaussian Splatting methods have evolved recently to learn neural networks that predict 3D Gaussians explaining a scene directly from a few images. We broadly categorize these methods into two categories:

Pose-Dependent Generalizable 3DGS: Several works assume input images come with known or precomputed poses (e.g., via SfM) and focus on designing architectures to infer 3D Gaussians from these posed views [3, 5, 15, 43, 52, 59, 63, 72]. A prominent example is pixelSplat [3], which introduced a two-view feed-forward network that utilizes epipolar cross attention transformer architecture to fuse multi-view information and predict per-pixel depth distribution for input images. These distributions are sampled to create a set of 3D Gaussian centers along the viewing rays. MVsplat [5] uses cost volume based fusion of multi-view information, adapting the Unimatch [62] architecture to regress for depth instead. Both methods use additional decoder heads to estimate rest of the 3D Gaussian parameters.

Pose-Free Generalizable 3DGS: An emerging frontier involves dispensing with known camera poses—allowing the network to infer scene geometry and camera registration jointly from images alone [28, 29, 48, 68]. Early efforts in this direction often build upon learned stereo matching. For example, [48] tackles uncalibrated stereo pairs by extending a foundation model (MASt3R [35]) that predicts dense point clouds from two images. It then outputs 3D Gaussians directly in a canonical frame, augmenting each point in the MASt3R reconstruction with color and covariance attributes. This process is supervised using the geometry of the 3D point cloud and followed by a novel-view synthesis stage to fine-tune appearance. NoPoSplat [68] adopts a more self-supervised, multi-view approach by anchoring one view’s coordinate system as canonical and training a network to predict all Gaussians directly in that space, using only a photometric loss for training.

To the best of our knowledge, all aforementioned generalizable splitting methods struggle to learn geometrically faithful orientations and scales for 3D Gaussians. The proposed approach alleviates this issue from generalizable splatting using appropriate geometric priors.

3. Method

In this section, we present our generalizable Gaussian splatting framework and loss functions we propose to address the ill-posed nature of self-supervised learning in predicting geometrically consistent Gaussians. For the architectural details, we refer the reader to the supplementary material.

Problem Definition. Assuming that we are given a set of sparse images $\mathcal{I} = \{\mathbf{I}_t \in \mathbb{R}^{H \times W \times 3}\}_{t=1}^T$ (which is also

known as context images in [3, 5, 29, 48, 63, 68]), each with known camera intrinsics that form the set $\mathcal{K} = \{\mathbf{K}_t \in \mathbb{R}^{3 \times 3}\}_{t=1}^T$ capturing a *rigid* scene, our aim is to learn a feedforward neural network f_Θ that maps these images and intrinsics $(\mathcal{I}, \mathcal{K})$ to a set of *pixel-aligned* Gaussians as:

$$f_\Theta(\mathcal{I}, \mathcal{K}) = \left\{ \mathcal{G}_t^j := \left(\boldsymbol{\mu}_t^j, \alpha_t^j, \mathbf{q}_t^j, \mathbf{s}_t^j, \mathbf{c}_t^j \right) \right\}_{t=1:T}^{j=1:H \times W}, \quad (1)$$

where \mathcal{G}_t^j is the 3D Gaussian defined in the 3D space corresponding to a pixel j in image t . Each \mathcal{G}_t^j is characterized by its *center* $\boldsymbol{\mu} \in \mathbb{R}^3$; *orientation* represented by a unit quaternion vector $\mathbf{q} \in \mathbb{R}^4$; three *scale* parameters $\mathbf{s} \in \mathbb{R}^3$ defining the elongation of the 3D Gaussians; *opacity* $\alpha \in \mathbb{R}$; and *color* encoded as spherical harmonics $\mathbf{c} \in \mathbb{R}^d$. In addition to the prevalent 3DGS representation adopted by generalizable Gaussian splatting frameworks [3, 5, 63, 68], we also explore the 2DGS representation introduced by [26], which models the scene with 2D surfels instead of standard 3D Gaussians. We present extensive evaluations and ablations quantifying the impact of this representation on generalizable Gaussian splatting in Section 4 and in the supplementary material.

Note that both Gaussian centers $\boldsymbol{\mu}_t^j$ and orientations \mathbf{q}_t^j are defined in the image coordinates of the *first* image \mathbf{I}_1 . Given these $M \times N \times T$ Gaussians predictions, we render *novel views* of the scene $\{\hat{\mathbf{I}}_f \in \mathbb{R}^{H \times W \times 3}\}_{f=1}^F \subset \mathcal{I}$ from F different viewpoints defined by its projection matrix $P_f = (\mathbf{R}_f, \mathbf{T}_f) \in \text{SE}(3)$ to be matched with its observed images \mathbf{I}_f s during training.

We minimize a view-synthesis loss [3, 5, 68] between the ground-truth image \mathbf{I}_f and the rendered image $\hat{\mathbf{I}}_f$:

$$\mathcal{L}_{\text{synthesis}} = \sum_{f=1}^F \left[\mathcal{L}_{\text{rgb}}(\mathbf{I}_f, \hat{\mathbf{I}}_f) + \mathcal{L}_{\text{lpips}}(\mathbf{I}_f, \hat{\mathbf{I}}_f) \right]. \quad (2)$$

For a pixel (u, v) in view f , the rendered color $\hat{\mathbf{I}}_f(u, v)$ is obtained by alpha-blending K depth-sorted projected Gaussians \mathcal{G}'_k :

$$\hat{\mathbf{I}}_f(u, v) = \sum_{k=1}^K \mathbf{c}_k w_k(u, v), \quad (3)$$

$$w_k(u, v) = T_k(u, v) \alpha_k \mathcal{G}'_k(u, v), \quad (4)$$

$$T_k(u, v) = \prod_{i < k} (1 - \alpha_i \mathcal{G}'_i(u, v)), \quad (5)$$

where \mathbf{c}_k and α_k denote the color and opacity of Gaussian k , and $\mathcal{G}'_k(u, v)$ is its 2D footprint in the image plane of \mathbf{I}_f (see supplementary material for details).

As shown in Section 4, solely relying on view synthesis loss is proven to be insufficient for learning geometrically meaningful Gaussians. In this work, we propose to minimize two additional regularization losses: (i) a depth-surface normal consistency term $\mathcal{L}_{\text{orient}}$ to align the orientations of

the Gaussians with dominant surface normal of the scene; (ii) a grid alignment loss $\mathcal{L}_{\text{align}}$ to ensure that the estimated Gaussians are aligned with the pixels of the provided images. Combining these two regularization with the view synthesis loss, we define our training objective function $\mathcal{L}_{\text{total}}$ as

$$\mathcal{L}_{\text{total}} = \mathcal{L}_{\text{synthesis}} + \lambda_o \mathcal{L}_{\text{orient}} + \lambda_a \mathcal{L}_{\text{align}}, \quad (6)$$

where λ_o and λ_a are weighting factors balancing the influence of each regularization (see Section 8). We discuss the motivation, formulation and impact of the regularization term in the following sections.

3.1. Learning Gaussian’s Orientations

Recall that existing pose-free and pose-aware generalizable Gaussian splatting approaches struggle to learn meaningful Gaussian orientations; see Figure 2. To endow the orientations with geometric meaning, we align them with the dominant surface normals of the underlying scene.

In both the 3DGS and 2DGS parameterizations, each Gaussian \mathcal{G}_t^j is associated with a covariance matrix

$$\Sigma_t^j = \mathbf{R}(\mathbf{q}_t^j) \text{diag}([s_t^{j,1}, s_t^{j,2}, s_t^{j,3}]^\top) \mathbf{R}(\mathbf{q}_t^j)^\top, \quad (7)$$

where $\mathbf{R}(\mathbf{q}_t^j) \in \text{SO}(3)$ is the rotation induced by the quaternion \mathbf{q}_t^j and $s_t^{j,1}, s_t^{j,2}, s_t^{j,3} \geq 0$ denote the axis-aligned scales in the local Gaussian frame. We define the *Gaussian normal* \mathbf{N}_t^j as the unit eigenvector of Σ_t^j corresponding to its smallest eigenvalue (equivalently, the column of $\mathbf{R}(\mathbf{q}_t^j)$ associated with $\arg \min_k s_t^{j,k}$).

In the 2DGS variant [26], each Gaussian is surfel-like and is parameterized by only two in-plane scales. For notational consistency with Equation (7), we represent this by appending a third scale fixed to zero, i.e., we set $s_t^{j,3} = 0$ in the diagonal of Σ_t^j . This yields a rank-deficient covariance whose null-space direction defines \mathbf{N}_t^j as in [26] (and $\arg \min_k s_t^{j,k}$ is attained by the appended zero scale). While this 2DGS specialization reduces over-parameterization, the view-synthesis loss in Eq. (2) still provides only weak supervision for learning orientations, for both 3DGS and 2DGS. A natural alternative is the rendered normal–depth consistency regularizer from [26]; however, naively deploying this rasterization-based regularizer in our generalizable setting does not yield stable training. We analyze this behavior and discuss remedies in the supplementary material.

Orientation supervision from local geometry. Instead, we directly supervise orientations using local surface normals estimated from neighboring Gaussian means. Assuming each Gaussian \mathcal{G}_t^j is aligned with pixel $j = (u, v)$ in frame t , we define central differences

$$\begin{aligned} \Delta_x \boldsymbol{\mu}_t^{(u,v)} &= \boldsymbol{\mu}_t^{(u+1,v)} - \boldsymbol{\mu}_t^{(u-1,v)}, \\ \Delta_y \boldsymbol{\mu}_t^{(u,v)} &= \boldsymbol{\mu}_t^{(u,v+1)} - \boldsymbol{\mu}_t^{(u,v-1)}, \end{aligned} \quad (8)$$

and compute a *local surface normal* from the corresponding 3D points as

$$\hat{\mathbf{N}}_t^j = \left\| \Delta_y \boldsymbol{\mu}_t^{(u,v)} \times \Delta_x \boldsymbol{\mu}_t^{(u,v)} \right\|_*, \quad (9)$$

where $\|\cdot\|_*$ denotes vector normalization and $\boldsymbol{\mu}_t^{(u,v)}$ is the 3D mean of the Gaussian aligned with pixel (u, v) .

Edge-aware orientation loss. Normals derived from local finite differences are least reliable at depth discontinuities. To reduce the influence of such pixels, we use an edge-aware weight based on the local 3D variation:

$$\begin{aligned} d_t^j &= \|\Delta_x \boldsymbol{\mu}_t^{(u,v)}\|_2 + \|\Delta_y \boldsymbol{\mu}_t^{(u,v)}\|_2, \\ \eta &= \text{Quantile}_q(\{d_t^j\}), \\ w_t^j &= w_0 \exp(-\kappa d_t^j / (\eta + \epsilon)), \end{aligned} \quad (10)$$

with fixed constants (w_0, κ) , q -quantile normalization, and a small ϵ for stability (see Section 8). We then encourage the predicted Gaussian normal \mathbf{N}_t^j (smallest-eigenvalue direction for 3DGS, null-space direction for 2DGS) to agree with $\hat{\mathbf{N}}_t^j$ using a Huber penalty in cosine space:

$$\mathcal{L}_{\text{orient}} = \frac{1}{|\Omega|} \sum_{(t,j) \in \Omega} w_t^j \mathcal{H}_\delta(1 - \langle \mathbf{N}_t^j, \hat{\mathbf{N}}_t^j \rangle), \quad (11)$$

where $\langle \cdot, \cdot \rangle$ denotes the dot product, $\mathcal{H}_\delta(\cdot)$ is the Huber loss with threshold δ , and Ω denotes the set of valid interior pixels over all frames (excluding a one-pixel boundary where central differences are undefined), i.e., $|\Omega| = T(H-2)(W-2)$.

Unlike rasterization-based priors, $\mathcal{L}_{\text{orient}}$ depends only on the predicted Gaussian means and covariances, providing direct supervision of orientation given $\boldsymbol{\mu}_t^j$. This formulation is representation-agnostic and applies equally to 3DGS and 2DGS. Conceptually, it mirrors supervised surface-normal training [12], where reference normals are derived from depth via Equation (9). In our experiments, this simple formulation consistently outperforms alternative orientation regularizers and can also be used in depth-supervised training of generalizable Gaussian splats.

Scale regularization (3DGS only). In our 3DGS variant, we additionally apply an anisotropy bias on the Gaussian scales to discourage near-isotropic covariances. Concretely, we add a penalty on the minimum per-Gaussian scale,

$$\begin{aligned} \mathcal{L}_{\text{flat}} &= \frac{1}{\mathcal{P}} \sum_{t,u,v} \min(s_t^{(u,v),1}, s_t^{(u,v),2}, s_t^{(u,v),3}), \\ \mathcal{L}_{\text{total}} &\leftarrow \mathcal{L}_{\text{total}} + \lambda_{\text{flat}} \mathcal{L}_{\text{flat}}. \end{aligned} \quad (12)$$

where the scales are those used in Equation (7), λ_{flat} is the weight, and $\mathcal{P} = TWH$ is the total number of pixel-aligned Gaussians in the scene. Unless stated otherwise, for 3DGS we apply this term together with the orientation loss (i.e., whenever $\mathcal{L}_{\text{orient}}$ is enabled). This term is disabled for 2DGS, where $s_t^{(u,v),3} = 0$ by construction.

3.2. Pixel-aligned Gaussians

Although the first generalizable splatting approach [3] operates in a pose-aware setup and adapts a two-view depth prediction network, it by construction constrains every Gaussian to lie on its corresponding viewing ray. Pose-free variants [68] drop the camera-pose assumption by directly estimating Gaussian locations in a canonical space using a DPT decoder. While this removes the need to warp Gaussians with known cameras, the resulting parameterization renders structure estimation ill-posed, especially in the self-supervised regime. In contrast to depth-supervised frameworks such as DUS3R [58], which learn an implicit structural prior by enforcing the reconstructed 3D point cloud to project onto a regular image grid, the pure view-synthesis loss in Eq. (2) does not impose such a constraint. Gaussians can therefore move freely into geometrically degenerate configurations, degrading both structure and relative pose estimation, while still explaining the input appearance.

We therefore explicitly align each Gaussian with its pixel’s viewing ray. Concretely, for each pixel (u, v) in frame t , the Gaussian center $\mu_t^{(u,v)}$ should reproject to (u, v) under the corresponding camera intrinsics \mathbf{K}_t and extrinsics $(\mathbf{R}_t, \mathbf{T}_t)$. We enforce this constraint with the alignment loss

$$\mathcal{L}_{\text{align}} = \frac{1}{\sum_{t,u,v} \mathcal{M}_t^{(u,v)}} \sum_{t=1}^T \sum_{u=1}^W \sum_{v=1}^H \mathcal{M}_t^{(u,v)} \ell_{\text{align}}(u, v, t), \quad (13)$$

$$\ell_{\text{align}}(u, v, t) = \| [u \ v]^\top - \Pi(\mathbf{K}_t [\mathbf{R}_t \mid \mathbf{T}_t] \tilde{\mu}_t^{(u,v)}) \|_2^2, \quad (14)$$

where $\tilde{\mu}_t^{(u,v)} = \left[(\mu_t^{(u,v)})^\top \ 1 \right]^\top$, $\mathcal{M}_t^{(u,v)} = 1$ if the projected mean lies within the image bounds and has positive depth (and 0 otherwise), and $\Pi([X, Y, Z]^\top) = [X/Z, Y/Z]^\top$ denotes the perspective projection.

As shown in Section 4, $\mathcal{L}_{\text{align}}$ plays an important role in PnP-based relative pose estimation (Tables 1 and 2) as well as accurate depth/structure estimation (Table 3).

4. Experiments

Datasets and implementation details. Following [3, 5, 68], we train our models on the large-scale RealEstate10K [75] (RE10K) dataset, with the train-test splits used by [68]. RE10K comprises predominantly indoor real-estate videos from YouTube, containing 67,477 training and 7,289 testing scenes, with camera poses computed using COLMAP [46]. For evaluating generalization, we further test on two additional datasets: ACID [40], containing aerial nature scenes captured by drones (with COLMAP-computed poses), and ScanNet [9], an RGB-D indoor scene dataset with distinct camera motion and characteristics. Specifically, we evaluate relative pose and geometry (depth and mesh) estimation on

the ScanNet. Our training broadly follows recent generalizable splatting methods; see supplementary material for full details.

4.1. Relative Pose Evaluation

Relative pose is evaluated by computing the AUC of the cumulative pose error curve at three thresholds. We report results deploying a PnP + RANSAC algorithm to align the Gaussian means with image grid as proposed in DUS3R[58]. NoPoSplat [68] proposes a gradient-descent relative pose refinement in which the predicted Gaussians are rendered to generate optimal input image pairs for refining the pose obtained by PnP+RANSAC. Pose Jacobians from [41] are used for this refinement over a fixed number of iterations.

Table 1 compares relative pose estimation performance across methods that do not require pose at inference (pose-free). CoPoNeRF [25] is trained on RE10K and ACID with explicit pose supervision. DUS3R [58] leverages indoor RGB-D and Internet SfM datasets (e.g., ScanNet++ [69], MegaDepth [38]) with a 3D regression objective supervising both depth and camera pose. MAST3R [35] follows a similar regime but additionally includes large-scale outdoor sequences from the Waymo Open Dataset [50]. RoMA [11] is trained on MegaDepth and ScanNet with joint depth-and-pose supervision. In contrast, our models use no explicit depth supervision and are trained solely on RE10K. Despite this, we outperform all these methods by a large margin, both on the in-domain RE10K test set and in zero-shot evaluations on ACID and ScanNet. The sole exception is RoMA [11] on ScanNet, the dataset it was explicitly trained on for relative pose estimation.

Compared to NoPoSplat, our method yields substantial relative-pose gains using only PnP+RANSAC. Incorporating the alignment loss $\mathcal{L}_{\text{align}}$ produces marked improvements in both in-domain and cross-domain zero-shot tests, while the orientation loss $\mathcal{L}_{\text{orient}}$ provides a further pose-estimation boost, with the combined full loss achieving the best performance. As in NoPoSplat, minimizing the input-image synthesis loss also benefits our pose estimation. Although gains on RE10K and ACID were modest, we observe proportionally larger improvements on ScanNet with this optimization. We refer the reader to the supplementary material for full implementation details and additional ablations of our losses under different pose estimation settings.

To further assess the quality of the predicted Gaussians structure under our proposed losses, we use pose estimation via PnP-only (least-squares optimization, without RANSAC) as a proxy for structure evaluation. Specifically, we estimate the relative pose between input views for both 3DGS and 2DGS representations on RE10K and ScanNet, as reported in Table 2. We deliberately use PnP-only in this comparison to more clearly expose structural differences: RANSAC’s outlier rejection can otherwise mask the impact of our priors.

Table 1. **Pose estimation (AUC) at multiple error thresholds on RE10K [75] (in-domain) and on ScanNet [9] and ACID [40] (cross-domain).** The overall best results are shown in **bold**, and the best result in each category is underlined. Methods marked with \dagger are trained on additional data (e.g., ScanNet, ScanNet++, ACID), and those marked with \ddagger use extra supervision (e.g., ground-truth depth). \wedge indicates evaluation with PnP+RANSAC only (no photometric pose refinement).

Pose Estimation Method	Method	RE10K			ScanNet			ACID		
		5° \uparrow	10° \uparrow	20° \uparrow	5° \uparrow	10° \uparrow	20° \uparrow	5° \uparrow	10° \uparrow	20° \uparrow
CoPoNeRF \dagger [25]	CoPoNeRF \dagger [25]	0.161	0.362	0.575	-	-	-	0.078	0.216	0.398
	DUST3R $\dagger\ddagger$ [58]	0.301	0.495	0.657	0.085	0.210	0.398	0.166	0.304	0.437
	MASt3R $\dagger\ddagger$ [35]	0.372	0.561	0.709	0.083	0.200	0.381	0.234	0.396	0.541
	RoMa $\dagger\ddagger$ [11]	0.546	0.698	0.797	0.168	0.361	0.575	0.463	0.588	0.689
PnP+RANSAC	Splatt3R \dagger [48]	0.158	0.325	0.504	0.011	0.042	0.119	0.044	0.121	0.260
	SelfSplat [29]	0.030	0.083	0.180	0.030	0.098	0.254	0.064	0.153	0.283
	NoPoSplat \wedge [68]	0.572	0.728	0.833	0.078	0.198	0.394	0.337	0.497	0.646
	Ours (3DGS+Align+Orient)	<u>0.629</u>	<u>0.770</u>	<u>0.858</u>	<u>0.124</u>	<u>0.282</u>	<u>0.493</u>	<u>0.404</u>	<u>0.560</u>	<u>0.689</u>
w/ Refinement (same loss as train)	SelfSplat [29]	0.031	0.086	0.182	0.033	0.112	0.274	0.069	0.156	0.285
	NoPoSplat [68]	0.672	0.791	0.868	0.109	0.256	0.463	0.456	0.593	0.705
	Ours (3DGS+Align+Orient)	0.684	0.801	0.875	<u>0.148</u>	<u>0.326</u>	<u>0.540</u>	0.466	0.598	0.713

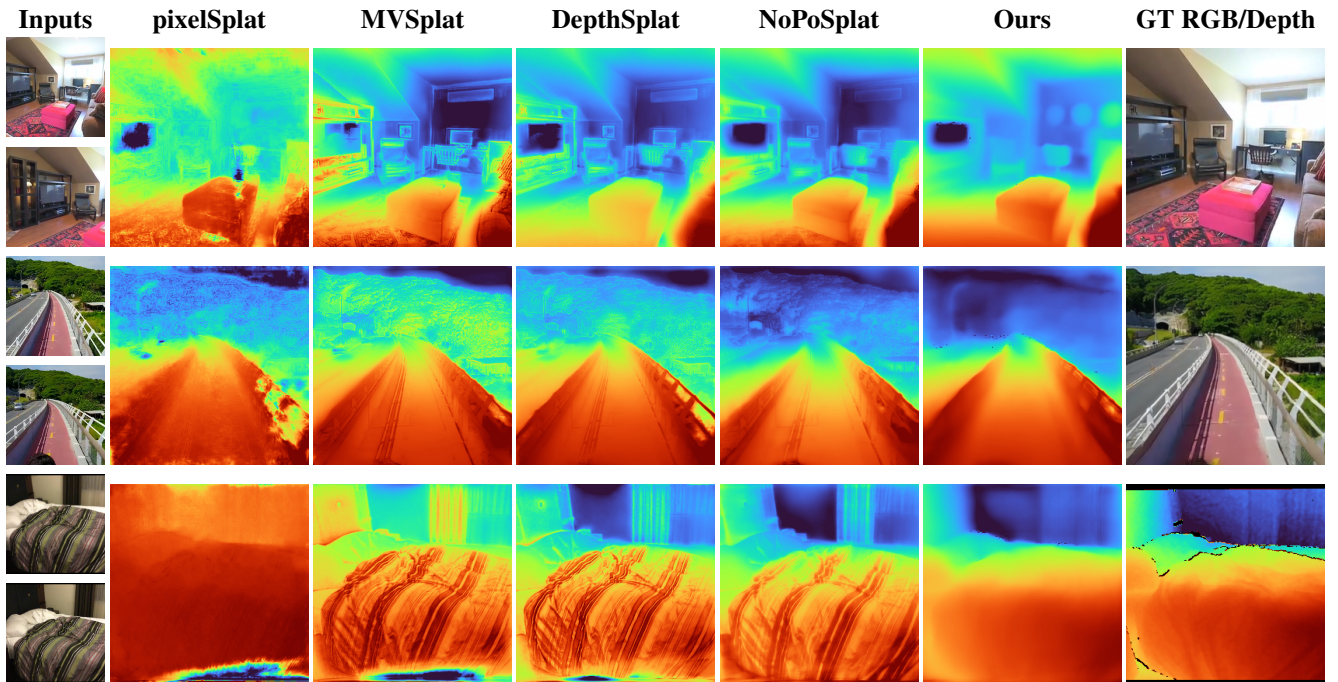


Figure 3. Qualitative comparison of rendered novel-view depth on RE10K (first row), ACID (second row), and ScanNet (last row).

We report average translation and rotation errors (in degrees), where the (scale-invariant) translation error is defined as the angular difference between normalized predicted and ground-truth translation vectors. The results show that our priors yield significantly lower translation and rotation errors, indicating more accurate Gaussian mean predictions compared to the baseline without priors. All comparisons are conducted under identical hyper-parameter settings.

4.2. Geometry Evaluation

Geometric veracity of the estimated 2D/3D Gaussian splats is the key focus of this work. Traditionally, the geometry predicted by neural networks is evaluated by measuring the depth errors for the input views. However, input depths do not capture the interpolation capability of predicted Gaussians and are insensitive to the opacity, orientation, and scale.

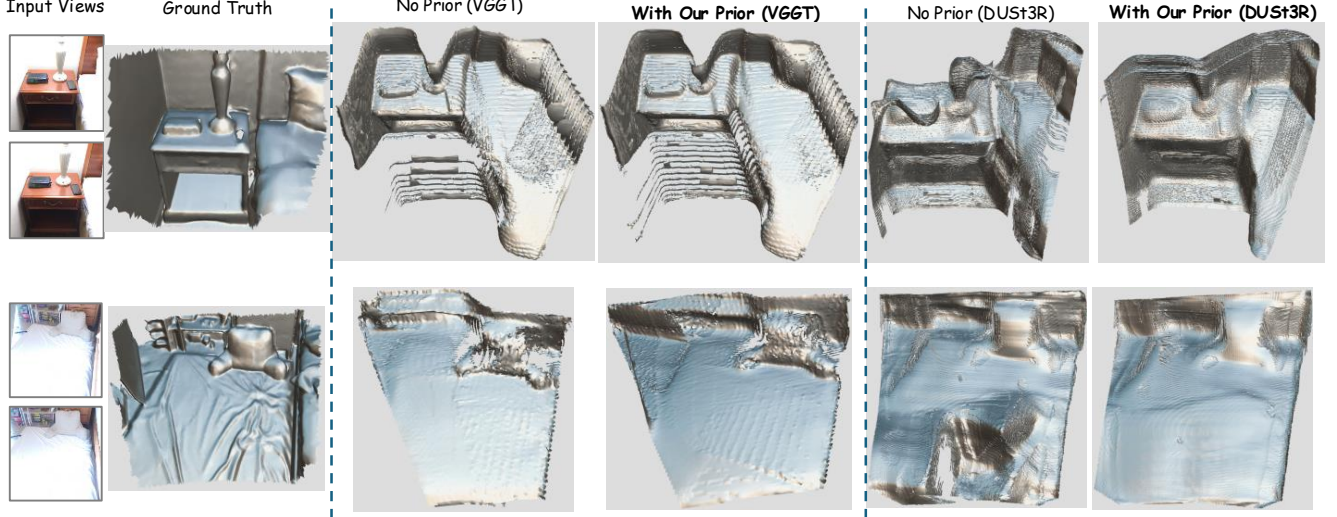


Figure 4. **Qualitative ablation of reconstructed meshes on ScanNet [9]** (2 input views) using VGGT [56] and DUST3R [58] backbones. Our proposed priors consistently yield sharper, more complete, and less noisy geometry across both backbones.

Table 2. **Ablation of pose-estimation translation and rotation errors using PnP (least squares).**

Estimation Method	Method	RE10K		ScanNet	
		Trans.↓	Rot.↓	Trans.↓	Rot.↓
PnP (LS)	3DGs (No Prior)	27.423	37.560	56.839	144.950
	Ours (3DGs+Align)	11.504	18.861	31.170	58.516
	Ours (3DGs+Orient)	10.689	18.626	31.108	55.403
	Ours (3DGs+Align+Orient)	10.594	18.587	30.848	55.294
	2DGs (No Prior)	29.693	47.225	54.057	82.707
	Ours (2DGs+Align)	15.667	23.619	23.271	11.729
	Ours (2DGs+Orient)	34.414	116.029	67.849	60.254
	Ours (2DGs+Align+Orient)	8.495	17.420	31.474	60.480

We propose a more holistic evaluation of the predicted scene structure by rendering multiple virtual depth maps from the reconstructed Gaussians and reporting Absolute Relative Error and depth accuracy for two different thresholds. As we do not aim to extrapolate beyond the given view frustum, we use the same view-synthesis test set for depth evalua-

Table 3. **Depth estimation on ScanNet [9]: novel vs. source views.** We report novel- and source-view depth accuracy side by side for each metric. A dash (–) indicates a metric is not applicable.

Method	Abs Rel ↓		$\delta_1 < 1.10 \uparrow$		$\delta_1 < 1.25 \uparrow$		
	Novel	Source	Novel	Source	Novel	Source	
Supervised DUST3R [58]	–	0.059	–	0.886	–	0.967	
Pose-required	pixelSplat [3]	0.299	0.288	0.552	0.553	0.818	0.820
	MVSplat [5]	0.189	0.132	0.412	0.641	0.745	0.891
	FreeSplat [59]	0.126	0.124	0.556	0.556	0.831	0.833
	DepthSplat [63]	0.135	0.105	0.578	0.722	0.864	0.914
Pose-free	Splat3R [48]	0.148	–	0.546	–	0.806	–
	SelfSplat [29]	0.160	0.155	0.502	0.460	0.810	0.801
	NoPoSplat [68]	0.131	0.121	0.554	0.662	0.851	0.869
	Ours (3DGs+Align+Orient)	0.090	0.082	0.713	0.740	0.916	0.928

Table 4. **Depth estimation ablation on ScanNet [9]: novel views.** Gray columns use the test-time pose refinement scheme (same loss as training) prescribed in [68].

Model	Abs Rel ↓		$\delta_1 < 1.10 \uparrow$		$\delta_1 < 1.25 \uparrow$	
	w/o	w/	w/o	w/	w/o	w/
<i>3DGs representation</i>						
3DGs (No Prior)	0.106	0.102	0.688	0.715	0.897	0.901
Ours (3DGs+Align)	0.097	0.089	0.701	0.729	0.907	0.920
Ours (3DGs+Orient)	0.093	0.085	0.707	0.733	0.913	0.925
Ours (3DGs+Align+Orient)	0.090	0.083	0.713	0.738	0.916	0.928
<i>2DGs representation</i>						
2DGs (No Prior)	0.121	0.114	0.668	0.692	0.879	0.884
Ours (2DGs+Align)	0.107	0.099	0.684	0.713	0.894	0.908
Ours (2DGs+Orient)	0.097	0.090	0.704	0.726	0.909	0.920
Ours (2DGs+Align+Orient)	0.094	0.082	0.715	0.743	0.916	0.931

tion. Virtual depth maps are rendered using the ground-truth relative pose w.r.t the first input frame, assuming perfectly aligned multi-view Gaussians. This puts pose-free methods at a severe disadvantage – small pose alignment errors amplify depth errors – yet they outperform pose-aware counterparts by a large margin, as shown in Table 3. Our approach substantially outperforms the baselines. As shown by the ablations in Table 4, the alignment and orientation losses provide markedly larger gains. In particular, we observe that $\mathcal{L}_{\text{align}}$ alone is insufficient to learn stable Gaussian orientations, whereas adding $\mathcal{L}_{\text{orient}}$ enforces geometry-consistent orientations and yields sharper novel-view renderings (color, depth, and surface normals), see supp. for details.

We compare novel-view depth estimation of our method against pixelSplat [3], MVSplat [5], NoPoSplat [68] and DepthSplat [63] in Figure 3. MVSplat, DepthSplat and NoPoSplat depths are hypersensitive to texture, while pixelSplat produces notably noisier depths in textureless regions. In

contrast, our method yields more plausible depths despite not requiring relative poses.

While our primary goal is to predict pixel-aligned, geometrically consistent Gaussians for novel-view depth rendering, we also benchmark source-view depth estimation accuracy of all baseline methods in Table 3. For each method, we report their best depth—whether rendered from Gaussians or predicted by their depth-estimation head—under its best-performing configuration. For example, pixelSplat attains its highest accuracy using rendered depth, whereas MVSplat and DepthSplat perform best with their network-predicted depths. Our method achieves the lowest AbsRel error and performs competitively in thresholded accuracy. More detailed results for one- and two-view depth prediction are provided in the supplementary material.

Mesh Evaluation. To further assess geometric consistency, we reconstruct scene meshes using only virtual novel views. For each scene, we first estimate a Gaussian-splatting representation from two source images; we then synthesize an interpolated camera trajectory between the sources, render per-view depth maps along this path, and fuse them with TSDF-Fusion [8] to obtain a surface mesh. We compare the reconstructed meshes (with and without our proposed priors) against the ground-truth meshes on ScanNet [9] using standard metrics [23, 76]: accuracy, completeness, and Chamfer distance. As shown in Table 5, our priors outperform the baselines across all metrics, indicating a consistent and accurate Gaussian-splatting representation of the scenes. Note that our model is not trained on ScanNet; all evaluations are zero-shot. Qualitative comparisons in Figure 4 further show that our priors yield more accurate and more complete reconstructions than the baselines for both DUS3R [58] and VGGT [56] backbone architectures. Additional details on the reconstruction protocol and metric computation are provided in the supplementary material.

Adaptation of VGGT. For our VGGT-based variant, we keep the pose and point-cloud branches of VGGT [56] intact and append an additional decoder that predicts Gaussian parameters. We train this splat predictor purely with a view-synthesis loss, without using the depth branch. Keeping spirit of self supervised structure learning, we remove the pseudo-depth supervision as used in [28]. We found that accounting for the different intrinsic and extrinsic parameter conventions used by VGGT is critical for stable training. To that end following [28] we include a pseudo-pose supervision term to keep the predicted camera parameters consistent. We evaluate VGGT-based splatting both with and without our proposed priors in Table 5. Figure 4 shows the reconstructed meshes obtained with and without deployment of prior on handpicked ScanNet scenes. From these results, it is clear that our quick adaptation of VGGT for learning 3D splat gives better results than the DUS3R-based adapta-

Table 5. **Mesh reconstruction ablation on ScanNet [9] (2 source views).** Under the TSDF-Fusion [8] protocol, our method significantly outperforms all baselines across all metrics.

	Acc \downarrow	Comp \downarrow	Chamfer Dist. \downarrow
No Prior (DUS3R)	0.266	0.514	0.390
With Our Priors (DUS3R)	0.255	0.498	0.377
No Prior (VGGT)	0.150	0.362	0.256
With Our Priors (VGGT)	0.139	0.349	0.244

tions presented before. Additionally, proposed priors indeed improve the VGGT based splat predictors both in terms of accuracy and completeness.

4.3. Novel View Synthesis Evaluation

We noted that the proposed method outperforms prior work in novel-view synthesis on the RE10K dataset, largely thanks to its warping-free formulation. Small improvements were observed due to priors (see supp. for detailed results).

5. Conclusion

We propose a novel self-supervised, generalizable splatting network that mitigates geometric inconsistencies in Gaussian splat recovery previously overlooked by the community. Our model produces state-of-the-art, geometrically consistent Gaussian splats from just two unposed images. While we train on RE10K using an asymmetric transformer architecture under self-supervision, our core contributions are invariant to these design choices. The priors introduced here will help future work on generalizable splatting and learning-based 3D scene recovery.

G³Splat: Geometrically Consistent Generalizable Gaussian Splatting

Supplementary Material

In this supplementary material, we first present additional quantitative and qualitative evaluations for both our DUS3R- (Section 6.2) and VGGT-based (Section 6.1) generalizable splatting variants. We then describe the underlying architectures for these backbones (Section 7), followed by implementation details (Section 8) and baseline protocols. Next, we discuss two key design choices: (i) rendered normal-depth consistency (Section 9) for the 2DGS variant and its relation to our proposed orientation prior, and (ii) the depth rendering strategy (Section 10) adopted in our model. We also discuss our pose refinement strategy in Section 11. Finally, we outline our mesh reconstruction and evaluation protocol (Section 12).

6. Additional Evaluations

6.1. Multi-view Results on VGGT-based Adaptation

Architecture of VGGT [56] offers the flexibility for easy adaptation of the trained splat predictor to be seamlessly used with single as well as large baseline multiple frames typically used in multi-view structure-from-motion (SfM) frameworks.

We train our VGGT-based splat predictor using only two context (source) views, without employing additional views for the view-synthesis loss (see Sections 7 and 8). Nevertheless, the resulting model can be applied *as is* in multi-view setups. We also find that the priors proposed in this work remain beneficial in this regime—and in fact become even more critical in this multi-view testing setup. To showcase the multi-view capabilities of the trained model, we select 24 test frames with non-degenerate baselines from the RE10K [75] test set, feed them jointly as input, and directly visualize the predicted Gaussians in Figure 6.

It can be seen that, similar to VGGT, our splat predictors generalize seamlessly to multi-view inputs. While the prior-free baseline trained only with a view-synthesis loss works out of the box, the visualizations reveal clear misalignment of Gaussian means across frames, indicating poor relative pose estimation in the vanilla VGGT adaptation. As a result, the predicted Gaussians are difficult to consolidate into a coherent, holistic 3D representation. Moreover, as the number of input views and the baseline increase, these misalignments accumulate and the baseline degrades further.

In contrast, when our priors are imposed, Gaussians from different frames are well aligned, indicating high out-of-the-box pose estimation accuracy. The predicted Gaussians can therefore be used directly as proxy 3D maps, without any post-processing heuristics such as bundle-adjustment-based pose correction. Even without pose refinement to fix mis-

alignments, our prior-augmented model produces Gaussians that yield high-fidelity renderings, whereas the baseline adaptation struggles and often produces distorted or smoothed-out novel views.

Figure 5 illustrates the effectiveness of our priors on a 150-view virtual museum sequence generated by Sora [44]. The baseline result exhibits noticeable trails from misaligned per-frame Gaussians, particularly near scene boundaries where the camera undergoes large motions. Even in regions with smoother camera motion, gradual drift in the Gaussians leads to smeared reconstructions (left). In contrast, the prior-assisted model is largely free from both large misalignments and small drifts, yielding cleaner geometry and sharper textures across most observed areas. Figure 7 further shows that these priors generalize to the out-of-domain Tanks and Temples dataset, despite being trained only on RE10K [75].

6.2. Additional Evaluations of the DUS3R-based Adaptation

6.2.1. Source View Depth from Single Image

Using Gaussian splats as a scene representation naturally supports both novel-view synthesis and holistic 3D reconstruction. While most generalizable splatting methods emphasize image interpolation between input views, our work places stronger focus on geometric consistency and full 3D reconstruction, with interpolation capabilities. On ScanNet [9], our Gaussian-splat-based approach achieves the best source-view depth accuracy among self-supervised splatting baselines (Table 3), particularly in terms of AbsRel, while remaining competitive with stronger supervised baselines. This motivates us to further examine whether replacing depth-map or point-cloud representations with Gaussian splats brings tangible benefits for source-view depth prediction.

As our method is fully self-supervised, the fairest comparison would be against other self-supervised approaches that take two uncalibrated views and are trained on RE10K [75]. However, such two-view self-supervised structure estimators are scarce. Instead, we evaluate on the well-studied single-view depth estimation setting, where a range of strong monocular baselines is available. We follow the DUS3R [58] single-view depth evaluation protocol by duplicating each input image into both views. As in Table 3, for each splatting-based baseline we report its best depth estimate in Table 6, choosing between depth rendered from Gaussians and depth read directly from pixel-aligned 3D Gaussian means.

In addition to splatting-based baselines, we include three state-of-the-art self-supervised single-view depth estima-

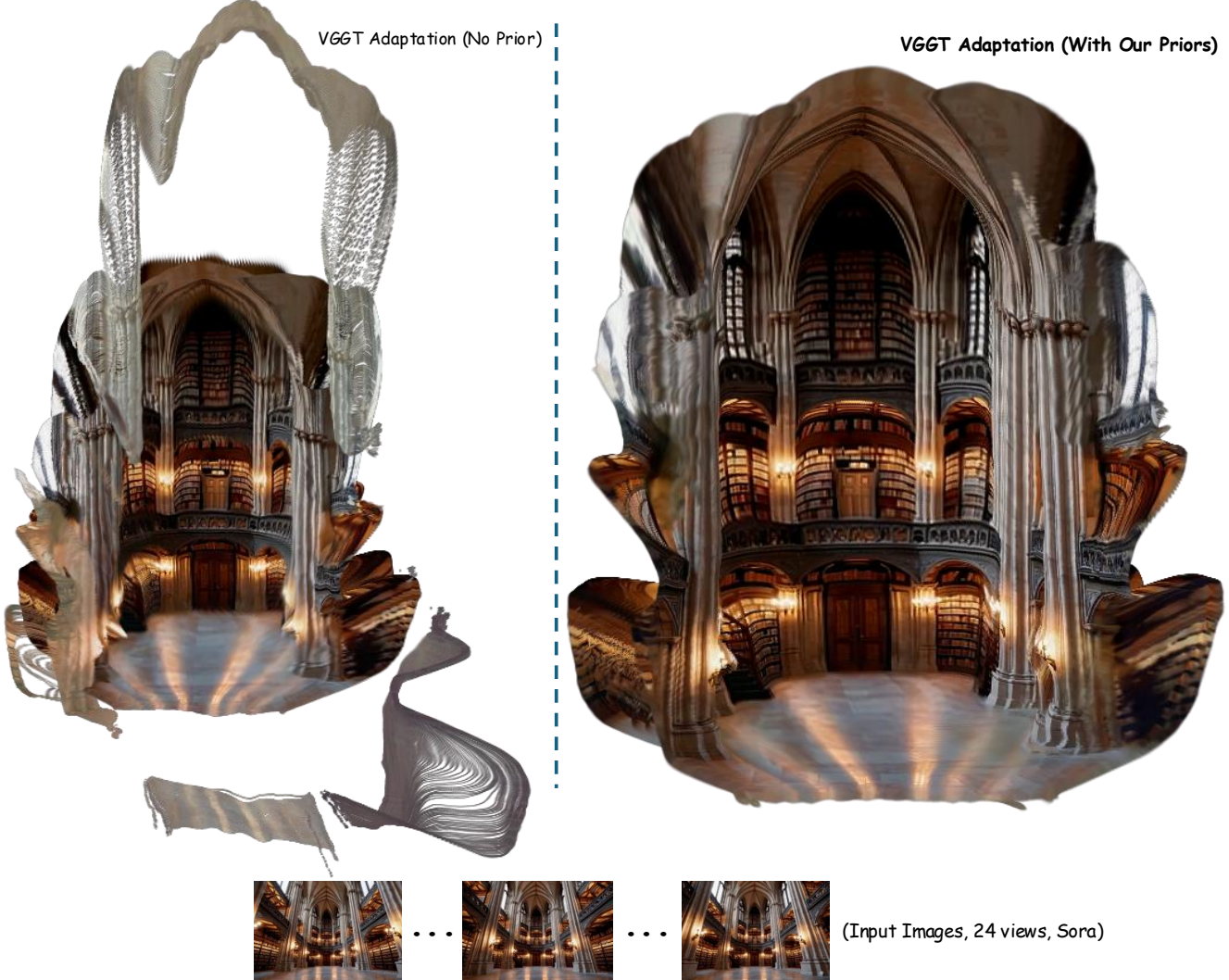


Figure 5. **Qualitative ablation of reconstructed Gaussians on a Sora-generated video (VGGT backbone, 24 input views).** Prompt used to generate the video: “A single unbroken orbital camera move through a vast, empty gothic library, with static architecture, medium-wide framing, warm steady lighting, and crisp sharp geometric details”.

tors: MonoDepthV2 [20], SC-SfM-Learners [1], and SC-DepthV3 [49]. On this NYUD-v2 [47] single-view benchmark, methods specifically designed for monocular depth generally perform strongest, as expected. Among the splatting-based approaches, DepthSplat [63] attains the best overall scores; this can be attributed in part to its use of a strong depth encoder (DepthAnything-V2 [64]) pretrained with dense depth supervision on a large corpus of depth datasets, giving it a significant advantage in this setting.

Within the family of self-supervised, two-view generalizable splatting methods, pixelSplat [3] struggles in the duplicated-view (zero-baseline) setting, while MVSplat [5] and NoPoSplat [68] provide much stronger baselines. Our best variant, Ours (3DGS+Align+Orient), matches or slightly improves upon NoPoSplat and the 3DGS no-prior baseline

across the reported metrics, while remaining competitive with classical self-supervised single-view methods. This experiment indicates that our geometric priors do not compromise, and in fact modestly improve, single-view depth quality within the pose-free splatting regime, even though our model is primarily optimized for multi-view reconstruction and pose estimation rather than specialized monocular depth prediction.

6.2.2. Novel-View Synthesis Evaluation

While novel-view synthesis is not the primary focus of this work, we evaluate both in-domain and zero-shot out-of-domain performance against relevant baselines (Table 7 and Table 8). For pose-free methods, novel views are rendered directly from all reconstructed Gaussians at a fixed



Figure 6. Qualitative ablation of reconstructed Gaussians on RE10K [75] (VGGT backbone, 24 input views).

target pose relative to the first input image. In contrast, methods that predict Gaussian means as depth maps require an additional warping step, using the ground-truth relative pose, to align Gaussians to the first-view coordinate frame. Although some works (e.g., [48]) report novel-view results for DUS3R [58] and MAST3R [35], these models are not designed for view synthesis, so we omit them from our depth and image-synthesis comparisons. Importantly, we do

not optimize camera poses for target-view image synthesis. While pose refinement is common in some NeRF and 3DGS pipelines, it can mask geometric inconsistencies and effectively “peek” at the ground truth during synthesis [6, 17], which we explicitly avoid here.

Our warping-free approach is consistently competitive with, and typically slightly outperforms, prior art in novel-view synthesis. Incorporating our proposed priors yields

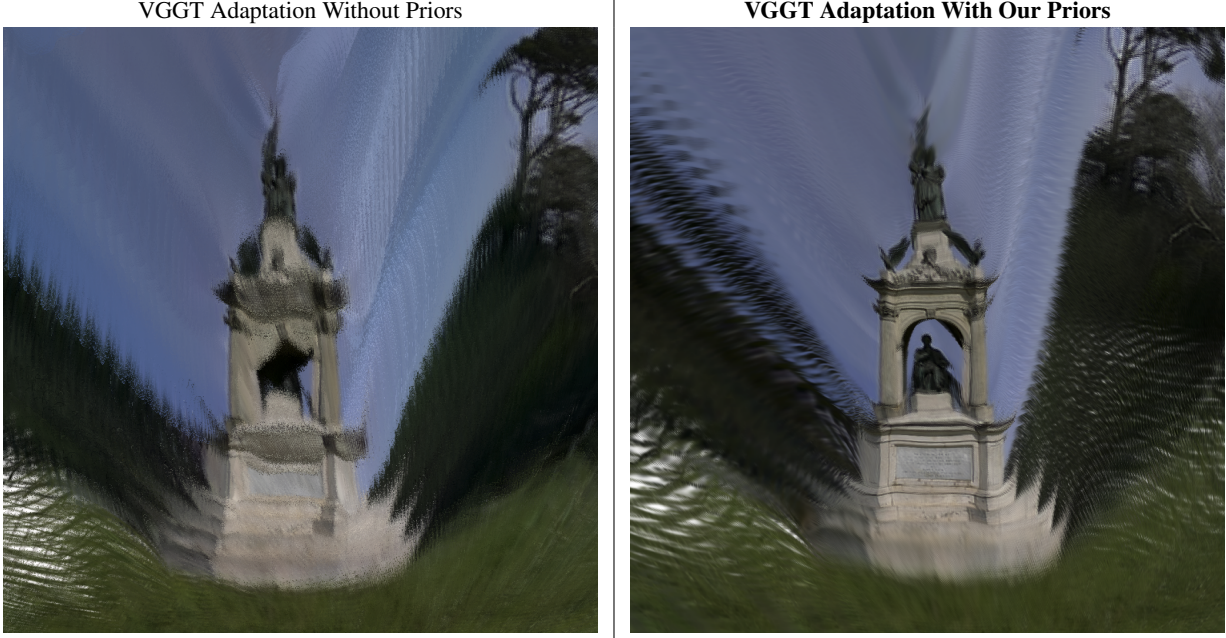
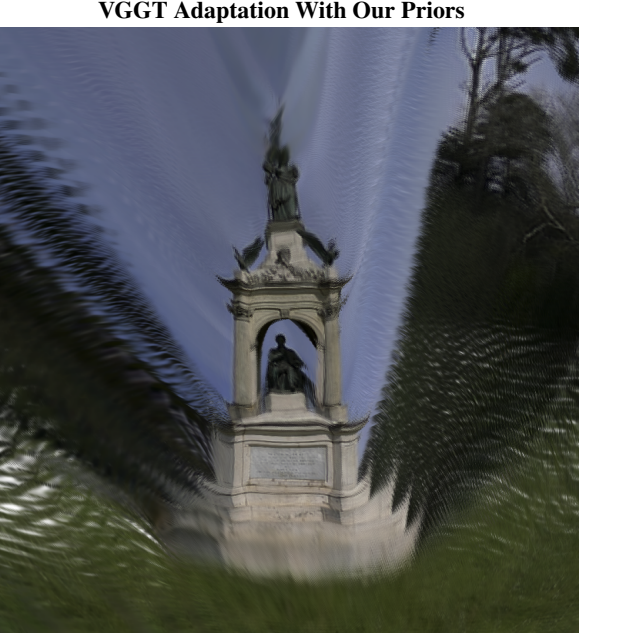


Figure 7. Qualitative ablation of reconstructed Gaussians on Tanks and Temples [32] (VGGT backbone, 20 input views).

Table 6. Single-view depth estimation results on NYUD-v2 [47]. Each scene is reconstructed from a single image, which is duplicated to form the two-view input required by our splatting-based estimators. For every splatting-based method, we report its “best depth estimate”, which may come either from rendered depth or from an intermediate depth prediction. We compare these against several state-of-the-art self-supervised single-view depth estimation methods, alongside the splatting-based baselines.

Training Scheme	Method	Best Source-View Depths		
		Abs Rel \downarrow	$\delta_1 < 1.10 \uparrow$	$\delta_1 < 1.25 \uparrow$
<i>Two-view Supervised</i>	DUST3R [58]	0.065	-	0.941
<i>Single-view Self-Supervised</i>	MonoDepthV2 [20]	0.162	-	0.745
	SC-SfM-Learners [1]	0.138	-	0.796
	SC-DepthV3 [49]	0.123	-	0.848
<i>Two-view Self-Supervised</i>	pixelSplat [3]	0.746	0.138	0.314
	MVSpplat [5]	0.281	0.277	0.574
	DepthSplat [63]	0.112	0.619	0.880
<i>Two-view Self-Supervised</i>	NoPoSplat [68]	0.172	0.423	0.749
	3DGs (No Prior)	0.172	0.425	0.750
	Ours (3DGs+Align)	0.190	0.396	0.720
	Ours (3DGs+Orient)	0.203	0.356	0.687
	Ours (3DGs+Align+Orient)	0.166	0.434	0.766

small but systematic improvements over pose-free methods on both RE10K [75] and ScanNet [9], with the largest quantitative gains observed on the out-of-domain ACID [40] benchmark. This behavior is consistent with our design goal: the priors are primarily intended to improve geo-



metric consistency (depth, pose, and mesh quality), and they achieve this without sacrificing—indeed, while slightly improving—novel-view image quality.

6.2.3. Additional Geometry Evaluations

In addition to the results in the main paper, we provide further qualitative comparisons of novel-view depth maps rendered by our method on RE10K [75] and ScanNet [9] in Figure 10.

We also report more detailed ablations of our proposed priors for both pose and depth estimation. For pose, Table 9 evaluates our models on RE10K [75], ScanNet [9], and ACID [40] under three schemes: PnP (least squares), PnP+RANSAC, and test-time photometric refinement (see Section 11 for details). For depth, Table 10 reports novel- and source-view depth error and accuracy on ScanNet [9].

Overall, the proposed priors yield substantial gains in geometric quality. In particular, under the PnP (least-squares) setting they almost double the pose AUC on RE10K (in-domain) and ACID (cross-domain), with even larger relative improvements on ScanNet, indicating fewer outliers and more reliable Gaussian means. Similarly, on ScanNet we observe more than a 20% reduction in absolute relative depth error for both novel and source views when both priors are enabled. These geometric improvements are also apparent in the reconstructed Gaussians on RE10K (Figure 8), which exhibit cleaner geometry and markedly fewer floating artifacts.

As discussed in the main paper, $\mathcal{L}_{\text{align}}$ alone is insufficient to learn stable Gaussian orientations. Adding $\mathcal{L}_{\text{orient}}$ enforces

Table 7. **Novel-view synthesis performance on RE10K [75].** We compare pose-required and pose-free methods against our model across different source-view overlap thresholds used in [68]. The best pose-free results (*without* target-pose optimization) are shown in **bold**, and the top pose-required method is underlined.

Method	Small			Medium			Large			Average			
	PSNR↑	SSIM↑	LPIPS↓	PSNR↑	SSIM↑	LPIPS↓	PSNR↑	SSIM↑	LPIPS↓	PSNR↑	SSIM↑	LPIPS↓	
Pose-Required	pixelNeRF [70]	18.417	0.601	0.526	19.930	0.632	0.480	20.869	0.639	0.458	19.824	0.626	0.485
	AttnRend [10]	19.151	0.663	0.368	22.532	0.763	0.269	25.897	0.845	0.186	22.664	0.762	0.269
	pixelSplat [3]	20.263	0.717	0.266	23.711	0.809	0.181	27.151	0.879	0.122	23.848	0.806	0.185
	MVSplat [5]	20.353	0.724	0.250	23.778	0.812	0.173	27.408	0.884	0.116	23.977	0.811	0.176
	FreeSplat [59]	19.411	0.691	0.277	22.839	0.790	0.192	26.433	0.869	0.130	23.026	0.788	0.196
Pose-Free	DepthSplat [63]	22.820	0.798	0.193	25.383	0.851	0.145	28.317	0.900	0.104	25.595	0.852	0.145
	Splatt3R [48]	14.352	0.475	0.472	15.529	0.502	0.425	15.817	0.483	0.421	15.318	0.490	0.436
	CoPoNeRF [25]	17.393	0.585	0.462	18.813	0.616	0.392	20.464	0.652	0.318	18.938	0.619	0.388
	SelfSplat [29]	15.557	0.572	0.435	19.648	0.703	0.301	24.142	0.817	0.191	19.931	0.704	0.303
	NoPoSplat [68]	21.097	0.723	0.237	23.191	0.779	0.187	25.107	0.817	0.144	23.244	0.778	0.187
	Ours (3DGS+Align+Orient)	21.221	0.731	0.235	23.347	0.785	0.185	25.418	0.826	0.141	23.417	0.783	0.185
	Ours (2DGS+Align+Orient)	21.377	0.739	0.234	23.426	0.787	0.184	25.459	0.827	0.141	23.504	0.787	0.184



Figure 8. **Qualitative ablation of reconstructed Gaussians on RE10K [75] (DUS3R backbone, 2 input views).**

Table 8. **Zero-shot out-of-distribution novel-view performance on ACID [40] and ScanNet [9].** We compare our models trained with the proposed priors for both 2DGS and 3DGS representations. All models are trained exclusively on the RE10K [75] dataset. Note that these results are obtained *without* optimizing camera poses for target views.

Method	ACID			ScanNet		
	PSNR↑	SSIM↑	LPIPS↓	PSNR↑	SSIM↑	LPIPS↓
NoPoSplat [68]	23.379	0.684	0.237	21.069	0.646	0.269
Ours (3DGS+Align+Orient)	23.763	0.700	0.236	21.137	0.648	0.269
Ours (2DGS+Align+Orient)	23.827	0.701	0.235	21.168	0.650	0.266

geometry-consistent normals and yields sharper novel-view renderings, as illustrated in Figure 9.

Finally, Figure 11 compares mesh reconstructions from two input views on ScanNet [9]. We evaluate pose-required baselines MVSplat [5] and DepthSplat [63], the pose-free NoPoSplat [68], and our method. Meshes are reconstructed

by fusing *virtual* (novel-view) rendered depth maps via TSDF-Fusion [8] (see Section 12 for details). For each method, we visualize Gaussian orientations (surface normals) for the first input view alongside the rendered depth for a novel view and its ground-truth depth. Our approach consistently produces geometrically coherent meshes, whereas competing methods' inconsistent novel-view depths often lead to deformed planar regions (rows one and three) and large holes (row two), losing fine scene detail.

7. Architectures

We instantiate our framework with two multi-view transformer backbones: a DUS3R-style [58] encoder (similar in spirit to [68]) and a VGGT-style generalist geometry transformer [56]. In both cases, the backbone produces per-image feature maps and multi-view aggregated features, and our Gaussian decoders predict per-pixel splat parameters (centers, scales, orientations, opacities, and colors) for 2DGS and 3DGS parameterizations. All variants are trained with

Table 9. **Pose estimation ablation of our method.** We report AUC at thresholds of 5° , 10° , and 20° on RE10K [75] (in-domain) and ScanNet [9] / ACID [40] (cross-domain). We evaluate both 2DGS and 3DGS models trained with the proposed priors under three pose estimation schemes: (i) PnP (least squares), (ii) PnP+RANSAC, and (iii) photometric test-time optimization (same loss as training). The best results within each pose estimation scheme are shown in **bold**.

Pose method	Model	RE10K			ScanNet			ACID		
		$5^\circ \uparrow$	$10^\circ \uparrow$	$20^\circ \uparrow$	$5^\circ \uparrow$	$10^\circ \uparrow$	$20^\circ \uparrow$	$5^\circ \uparrow$	$10^\circ \uparrow$	$20^\circ \uparrow$
PnP (LS)	3DGS (No Prior)	0.296	0.437	0.570	0.019	0.050	0.104	0.189	0.279	0.378
	Ours (3DGS+Align)	0.388	0.558	0.692	0.029	0.089	0.199	0.250	0.366	0.476
	Ours (3DGS+Orient)	0.477	0.642	0.753	0.068	0.141	0.221	0.296	0.414	0.508
	Ours (3DGS+Align+Orient)	0.482	0.645	0.753	0.052	0.121	0.209	0.301	0.416	0.511
	2DGS (No Prior)	0.223	0.344	0.487	0.008	0.026	0.076	0.154	0.237	0.339
	Ours (2DGS+Align)	0.338	0.519	0.668	0.031	0.083	0.176	0.229	0.341	0.453
	Ours (2DGS+Orient)	0.194	0.252	0.314	0.015	0.035	0.055	0.049	0.063	0.093
	Ours (2DGS+Align+Orient)	0.526	0.679	0.774	0.051	0.126	0.210	0.327	0.442	0.529
PnP+RANSAC	3DGS (No Prior)	0.572	0.728	0.833	0.078	0.198	0.394	0.337	0.497	0.646
	Ours (3DGS+Align)	0.594	0.742	0.840	0.090	0.222	0.431	0.344	0.506	0.650
	Ours (3DGS+Orient)	0.600	0.746	0.845	0.132	0.298	0.491	0.367	0.533	0.674
	Ours (3DGS+Align+Orient)	0.629	0.770	0.858	0.124	0.282	0.493	0.404	0.560	0.689
	2DGS (No Prior)	0.588	0.737	0.832	0.085	0.223	0.432	0.344	0.513	0.659
	Ours (2DGS+Align)	0.619	0.759	0.849	0.120	0.279	0.471	0.382	0.540	0.674
	Ours (2DGS+Orient)	0.592	0.743	0.836	0.099	0.241	0.448	0.374	0.535	0.672
	Ours (2DGS+Align+Orient)	0.629	0.768	0.856	0.128	0.281	0.477	0.387	0.546	0.682
w/ Refinement (same loss as train)	3DGS (No Prior)	0.672	0.791	0.868	0.109	0.256	0.463	0.456	0.593	0.705
	Ours (3DGS+Align)	0.680	0.797	0.871	0.129	0.284	0.513	0.460	0.596	0.709
	Ours (3DGS+Orient)	0.684	0.801	0.874	0.144	0.318	0.527	0.469	0.604	0.718
	Ours (3DGS+Align+Orient)	0.684	0.801	0.875	0.148	0.326	0.540	0.466	0.598	0.713
	2DGS (No Prior)	0.672	0.788	0.859	0.129	0.298	0.494	0.460	0.599	0.713
	Ours (2DGS+Align)	0.681	0.799	0.870	0.136	0.311	0.512	0.474	0.607	0.718
	Ours (2DGS+Orient)	0.675	0.793	0.869	0.130	0.301	0.503	0.466	0.601	0.714
	Ours (2DGS+Align+Orient)	0.686	0.802	0.875	0.153	0.334	0.541	0.478	0.609	0.723

Table 10. **Depth estimation ablation on ScanNet [9]: novel and source views.** Gray columns use the test-time pose refinement scheme (same loss as training) prescribed in [68].

Model	Novel view						Source view					
	Abs Rel \downarrow		$\delta_1 < 1.10 \uparrow$		$\delta_1 < 1.25 \uparrow$		Abs Rel \downarrow		$\delta_1 < 1.10 \uparrow$		$\delta_1 < 1.25 \uparrow$	
	w/o	w/	w/o	w/	w/o	w/	w/o	w/	w/o	w/	w/o	w/
<i>3DGS representation</i>												
3DGS (No Prior)	0.106	0.102	0.688	0.715	0.897	0.901	0.105	0.097	0.689	0.707	0.897	0.905
Ours (3DGS+Align)	0.097	0.089	0.701	0.729	0.907	0.920	0.089	0.086	0.729	0.740	0.918	0.923
Ours (3DGS+Orient)	0.093	0.085	0.707	0.733	0.913	0.925	0.085	0.083	0.733	0.742	0.925	0.928
Ours (3DGS+Align+Orient)	0.090	0.083	0.713	0.738	0.916	0.928	0.082	0.080	0.740	0.747	0.928	0.930
<i>2DGS representation</i>												
2DGS (No Prior)	0.121	0.114	0.668	0.692	0.879	0.884	0.118	0.105	0.665	0.705	0.875	0.894
Ours (2DGS+Align)	0.107	0.099	0.684	0.713	0.894	0.908	0.100	0.096	0.712	0.723	0.904	0.911
Ours (2DGS+Orient)	0.097	0.090	0.704	0.726	0.909	0.920	0.090	0.090	0.727	0.735	0.920	0.922
Ours (2DGS+Align+Orient)	0.094	0.082	0.715	0.743	0.916	0.931	0.086	0.079	0.736	0.752	0.925	0.934

the same view-synthesis objective and our proposed geometric priors; only the choice of backbone and aggregation

mechanism differs.

DUST3R-based variant. Our first instantiation builds on

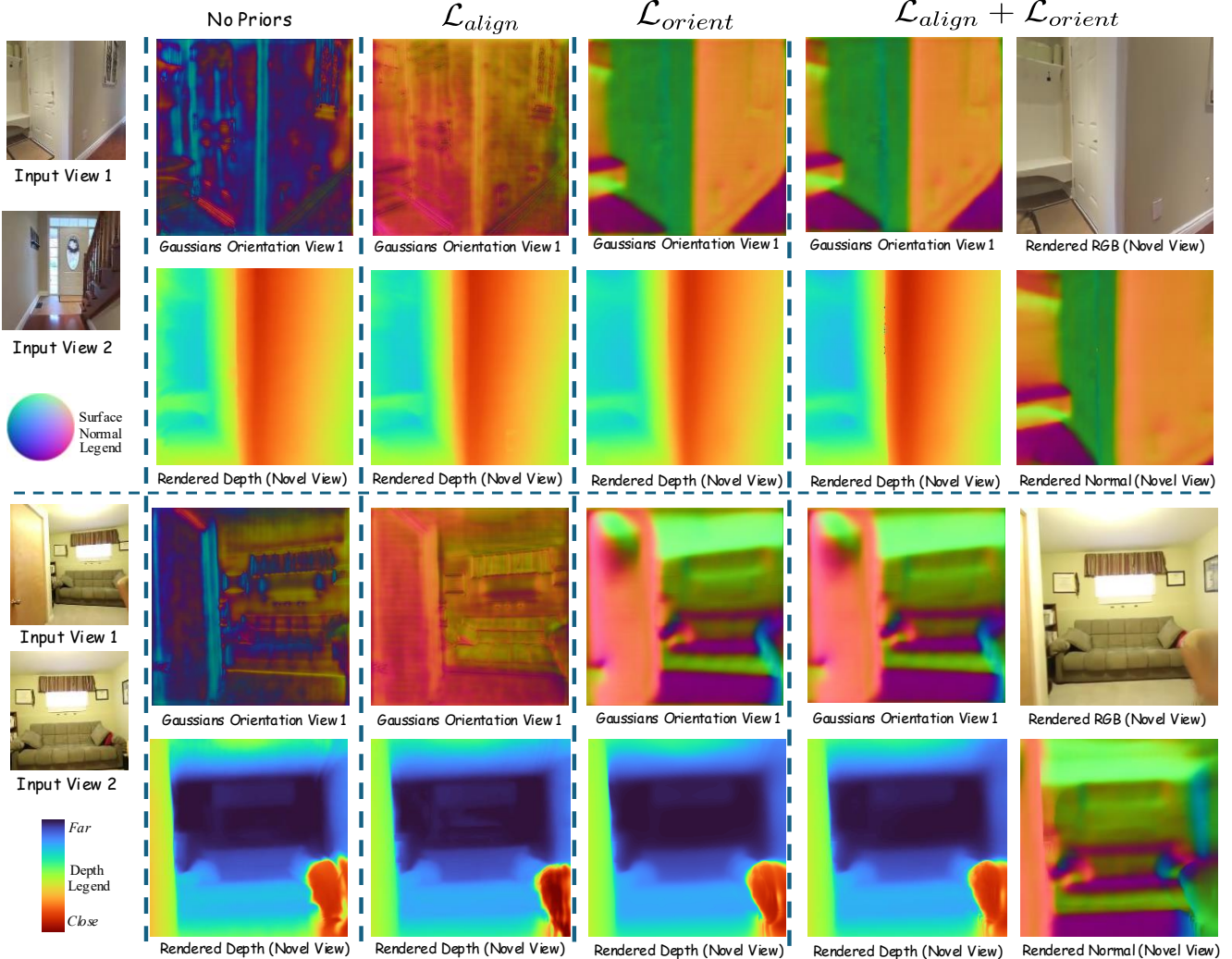


Figure 9. **Qualitative ablation of the losses.** We visualize the learned Gaussian orientations (from the first input view) along with rendered novel-view depth, color, and surface normals, on RE10K [75]. As shown, using $\mathcal{L}_{\text{align}}$ alone is insufficient to learn reliable Gaussian orientations; adding $\mathcal{L}_{\text{orient}}$ encourages geometry-consistent orientations and, together, they produce more accurate rendered depth.

the pose-free, N -view transformer design pioneered by DUS3R [58], which was also adopted in [68] for generalizable Gaussian splatting, and adapts it to predict Gaussian splats with our 2DGS/3DGS parameterizations and priors. The architecture comprises three main components: (i) a transformer-based image encoder, (ii) two asymmetric multi-view feature aggregators, and (iii) dense prediction decoders for Gaussian parameters.

The image encoder maps each RGB frame and its intrinsic parameters to a sequence of tokens (patch embeddings plus camera embeddings), which are processed independently by a ViT encoder. The resulting per-view features are then fused by two sets of cross-attention-based aggregators: one produces features for the reference (first) image, and the other produces features for the remaining images, conditioned

on the reference. This asymmetric aggregation follows the spirit of DUS3R, aligning all frames to a common canonical coordinate frame without requiring ground-truth poses.

Given the aggregated features, two DPT-style decoders predict Gaussian parameters. The first decoder regresses the Gaussian centers (i.e., 3D positions associated with each input pixel), while the second decoder predicts the remaining parameters (scales, orientations, opacities, and colors), optionally combining higher-resolution image features for appearance. Because all predicted Gaussians are expressed in a shared canonical frame, their union can be directly rendered from arbitrary viewpoints using the differentiable splatting pipeline, without explicit warping or known camera poses. Both the image tokenizer and the feature aggregators are built entirely from standard Vision Transformer blocks,

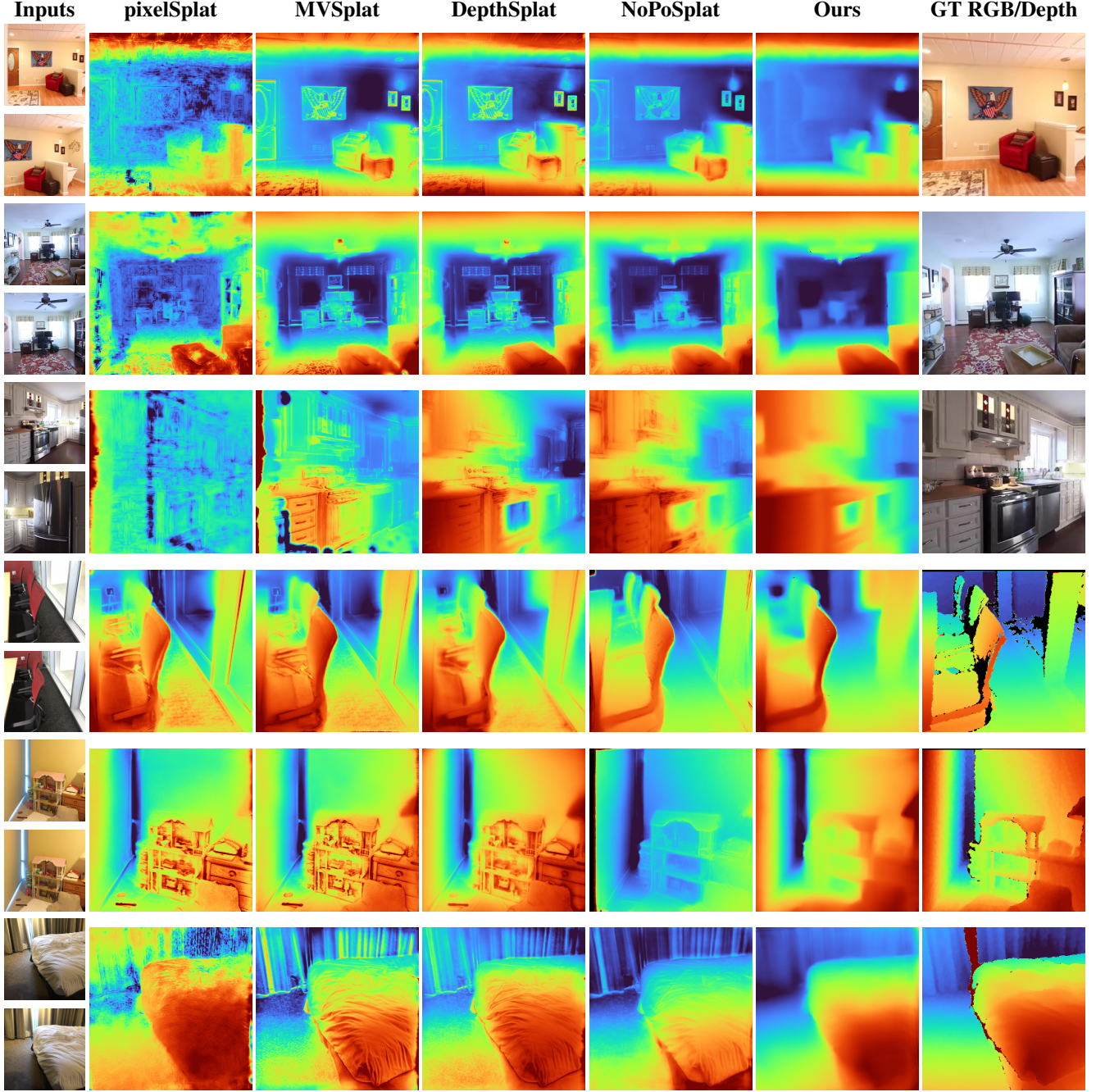


Figure 10. **More qualitative comparison of novel-view rendered depth on RE10K [75] and ScanNet [9].** pixelSplat depths are relatively geometrically consistent but noisy when the baseline is small. Large errors can be observed in the pixelSplat depths when the image overlap is small. Other baselines provide depth maps, which are hypersensitive to image texture. While some potentially meaningful fine structural edges are visible in these depth maps (see chair handles in row 4), the depth maps have many non-geometric “fake edges” (paintings in row 1, sofa in row 2, cabinet in row 3 – to name a few). Our method provides geometrically consistent renderings in all these scenarios.

without epipolar-specific attention or explicit multi-view cost volumes, keeping the architecture geometry-free and compatible with our priors.

VG GT-based variant. To demonstrate that our priors are not

tied to a specific backbone, we also instantiate the framework with a VG GT-style architecture [56], which jointly predicts camera poses and 3D structure from multiple views. We retain the original pose and point-cloud branches of VG GT

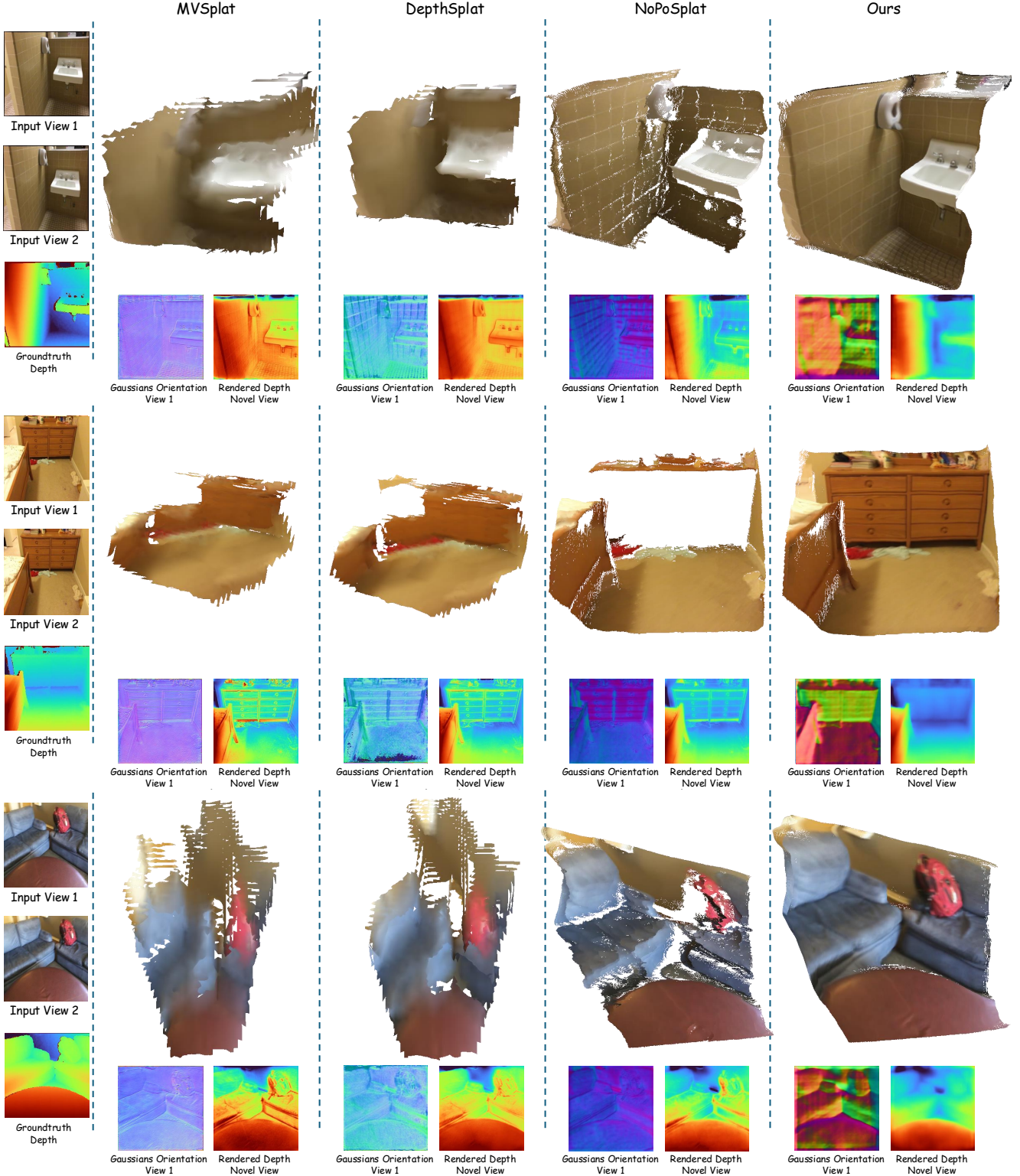


Figure 11. **Qualitative comparison of mesh reconstruction on ScanNet [9] (DUST3R backbone, 2 input views).** For each scene, we show the two input context views, the textured mesh reconstructed by fusing *virtual* rendered depth maps via TSDF-Fusion [8], the Gaussian normals for the first input view, and the ground-truth and rendered depth from a novel (virtual) viewpoint. Baselines exhibit inaccurate rendered depth and normals; when fused, these inconsistencies lead to holes and deformed regions in the reconstructed meshes.

and append an additional Gaussian-splat decoder that consumes the multi-view features to predict per-pixel Gaussian parameters. In this variant, the network is trained purely with a view-synthesis loss on the rendered Gaussians. The Gaussian decoder attached to VGGT mirrors the DUS3R-based variant: it predicts centers, scales, orientations, opacities, and colors for 3DGS splats, and is trained jointly with the backbone using our view-synthesis loss and geometric priors.

8. Implementation Details

Common training setup. All models are trained in a generalizable splatting regime on the RealEstate10K (RE10K) training split [75]. We use two input images per sample and render three virtual novel views to minimize the view-synthesis loss described in the main paper. The same loss weights are used across all architectures and ablations: the alignment and orientation priors are weighted by $\lambda_a = 0.1$ and $\lambda_o = 0.05$.

For the edge-aware weights in Equation (10), we set the robust scale to the $q=0.95$ quantile, i.e., $\eta = \text{Quantile}_{0.95}(\{d_q^j\})$. We use fixed constants $(w_0, \kappa) = (10, 4)$ and a small ϵ for numerical stability (we use $\epsilon = 10^{-8}$ in all experiments). For the cosine-space penalty in Equation (11), we use the Huber (SmoothL1) threshold $\delta = 0.1$. We apply the scale regularization $\mathcal{L}_{\text{flat}}$ only for the 3DGS variant, with a fixed weight $\lambda_{\text{flat}} = 1000$. All variants are evaluated on the same test splits and protocols described below. We will release the source code and pretrained models to facilitate reproducibility.

DUS3R-based variant. For the DUS3R-based backbone, training is performed on a cluster of 24 NVIDIA A100 (40 GB) GPUs with a batch size of 6 per GPU (144 total), while all evaluations are run on a single NVIDIA A6000 GPU. We train for 18,751 iterations on RE10K using the setup above, with input images resized to 256×256 . The Gaussian decoders are optimized with a base learning rate of 2×10^{-4} , and the DUS3R layers are updated with a reduced rate of 2×10^{-5} . In line with observations from [68], we found that training this architecture from scratch on RE10K is unstable in the fully self-supervised setting; instead, we initialize the backbone with MAST3R-pretrained weights [35] and fine-tune it jointly with our Gaussian decoders. Competing DUS3R-style baselines are allowed to use the same supervised backbone initialization for fairness. Under this setup, training the DUS3R-based variant on RE10K takes approximately 6 hours.

VGGT-based variant. For the VGGT-based backbone [56], we adopt the same dataset, number of source views, and number of rendered novel views as in the DUS3R-based setup. During training, we cap the longer image side at 448 pixels and randomly vary the aspect ratio between 0.5 and 1.0. The Gaussian decoder attached to VGGT is optimized

with a base learning rate of 2×10^{-4} , while the VGGT backbone is updated with a lower rate of 2×10^{-5} to preserve its pre-trained multi-view geometry priors. We initialize the backbone from VGGT pretrained weight and train the added Gaussian head end-to-end with our view-synthesis loss and geometric priors. The corresponding wall-clock training time for the VGGT-based variant is approximately 8 hours on a single GPU with a batch size of 36.

Evaluation protocols. To evaluate zero-shot generalization in pose estimation, geometry reconstruction, and novel-view synthesis, we use the same test sets and splits for all architectures and baselines. Specifically, we evaluate on the ACID split from [68] and on the ScanNet test set [9], which comprises 2000 indoor RGB-D image pairs. For ScanNet, novel views are obtained by uniformly sampling up to four intermediate viewpoints along the camera trajectory between each pair of source views used for pose evaluation, resulting in 1592 novel-view samples (out of 2000). These novel views are used consistently for both depth, mesh, and novel-view synthesis evaluations.

Baselines and retraining protocol. For all baselines, we use publicly released pretrained checkpoints whenever available. When multiple versions exist, we select models trained on RE10K [75] and at least at our input resolution of 256×256 ; if a model is trained on RE10K plus additional data or at higher resolution, we still use that checkpoint to give the baseline a slight advantage. If no RE10K-pretrained model is available (e.g., for FreeSplat [59]), we retrain the method following the authors' original training protocol and hyperparameters to ensure a fair comparison.

For NoPoSplat [68] specifically, we additionally retrain their model under our setup (RE10K dataset, iteration count, input resolution, and view-synthesis protocol). Minor deviations from the originally reported numbers are summarized in Table 11.

9. Rendered Normal for 2DGS

In this subsection, we revisit the rendered normal-depth consistency loss introduced by 2DGS [26] and compare it against our proposed orientation prior $\mathcal{L}_{\text{orient}}$. While $\mathcal{L}_{\text{orient}}$ is defined directly on Gaussian normals and can be applied to both 2DGS and 3DGS parameterizations, the 2DGS loss operates on *rendered* surface normals and thus can only be instantiated and ablated for our 2DGS variant, where we explicitly render per-pixel normals.

For a 3D Gaussian corresponding to pixel j in image t ,

$$\mathcal{G}_t^j = (\mu_t^j, \alpha_t^j, \Sigma_t^j, \mathbf{c}_t^j),$$

3DGS [31] first projects the mean and covariance to the image plane of a novel view. Let

$$\mathbf{P}_f = \mathbf{K}_f [\mathbf{R}_f \mid \mathbf{T}_f] \in \mathbb{R}^{3 \times 4}$$

Table 11. Comparison of our retrained NoPoSplat against the public checkpoint (NoPoSplat*). (a) Pose evaluation (with test-time photometric pose refinement) on RE10K [75], ScanNet [9] and ACID [40]. (b) Depth estimation for novel views (with pose refinement) on ScanNet. (c) Novel-view synthesis on RE10K.

(a) Pose evaluation										
Method	RE10K			ScanNet-V1			ACID			
	5° ↑	10° ↑	20° ↑	5° ↑	10° ↑	20° ↑	5° ↑	10° ↑	20° ↑	
NoPoSplat*	0.672	0.792	0.869	0.111	0.254	0.465	0.454	0.591	0.709	
NoPoSplat	0.672	0.791	0.868	0.109	0.256	0.463	0.456	0.593	0.705	

(b) Depth estimation										
Rendered Depth (Novel Views)										
Method	Abs Rel↓			$\delta_1 < 1.10 \uparrow$			$\delta_1 < 1.25 \uparrow$			
NoPoSplat*	0.127			0.564			0.859			
NoPoSplat	0.126			0.567			0.861			
Our baseline (No Prior 3DGS)	0.102			0.715			0.901			
Our baseline (No Prior 2DGS)	0.114			0.692			0.884			

(c) Novel-view synthesis												
Method	Small			Medium			Large			Average		
	PSNR↑	SSIM↑	LPIPS↓	PSNR↑	SSIM↑	LPIPS↓	PSNR↑	SSIM↑	LPIPS↓			
NoPoSplat*	21.086	0.721	0.237	23.134	0.776	0.185	25.086	0.818	0.141	23.189	0.775	0.185
NoPoSplat	21.097	0.723	0.237	23.191	0.779	0.187	25.107	0.817	0.144	23.244	0.778	0.187

be the projection matrix of view f . Dropping (t, j, f) for clarity, the homogeneous image of the mean is

$$\bar{\mu} = \mathbf{P} [\mu^\top 1]^\top, \quad \mu' = \begin{bmatrix} \bar{\mu}_x / \bar{\mu}_z \\ \bar{\mu}_y / \bar{\mu}_z \end{bmatrix}.$$

Denoting by

$$\mathbf{J} = \frac{\partial(\mu' \bar{\mu}_z)}{\partial \mu}$$

the Jacobian of the local affine approximation of the perspective map, the (unnormalized) screen-space covariance is

$$\Sigma' = \mathbf{J} \mathbf{P} \Sigma \mathbf{P}^\top \mathbf{J}^\top,$$

and we keep only its upper-left 2×2 block, $\Sigma'_{uv} = (\Sigma')_{1:2,1:2}$. The projected 2D Gaussian footprint is then

$$\mathcal{G}'(u, v) = \exp\left[-\frac{1}{2}((u, v)^\top - \mu')^\top \Sigma'_{uv}^{-1}((u, v)^\top - \mu')\right].$$

For a pixel (u, v) in view f , novel-view RGB is rendered via front-to-back α -blending of K depth-sorted Gaussians:

$$\hat{\mathbf{I}}_f(u, v) = \sum_{k=1}^K \mathbf{c}_k w_k(u, v), \quad (15)$$

$$w_k(u, v) = T_k(u, v) \alpha_k \mathcal{G}'_k(u, v), \quad (16)$$

with transmittance

$$T_k(u, v) = \prod_{j < k} (1 - \alpha_j \mathcal{G}'_j(u, v)).$$

The same weights $w_k(u, v)$ can be reused to render depth and surface normals for that view.

Rendered normal-depth consistency loss from 2DGS.

2DGS [26] proposes a *rendered normal-depth consistency* loss that enforces agreement between rendered surface normals and normals estimated from the rendered depth map. Let $\mathbf{x} = (u, v)^\top$ and let $D_r(\mathbf{x})$ denote the rendered depth obtained by combining per-Gaussian depths $d_k(\mathbf{x})$ with the same weights as color:

$$D_r(\mathbf{x}) = \sum_k w_k(\mathbf{x}) d_k(\mathbf{x}).$$

Let \mathbf{n}_k be the (unit) normal associated with Gaussian \mathcal{G}_k . The rendered normal is then

$$\mathbf{N}_r(\mathbf{x}) = \left\| \sum_k w_k(\mathbf{x}) \mathbf{n}_k \right\|_*,$$

where $\|\cdot\|_*$ denotes vector normalization. A corresponding normal $\widehat{\mathbf{N}}(\mathbf{x})$ can be estimated from $D_r(\mathbf{x})$ via finite differences and normalization. The rendered normal-depth consistency loss introduced in [26] penalizes the angular discrepancy between these two normals:

$$\mathcal{L}_{RNC} = \frac{1}{|\Omega|} \sum_{\mathbf{x} \in \Omega} \omega(\mathbf{x}) \left(1 - \langle \mathbf{N}_r(\mathbf{x}), \widehat{\mathbf{N}}(\mathbf{x}) \rangle \right), \quad (17)$$

where Ω is the set of valid pixels and

$$\omega(\mathbf{x}) = \sum_k w_k(\mathbf{x})$$

acts as an opacity-based confidence weight.

Comparison to our orientation prior. In our work, \mathcal{L}_{RNC} is not part of the final model; we implement it in the 2DGS variant purely as a baseline to compare against our proposed orientation prior $\mathcal{L}_{\text{orient}}$, which operates directly on Gaussian normals and is defined consistently for both 2DGS and 3DGS parameterizations. As discussed in the main paper, \mathcal{L}_{RNC} acts *after* rasterization and thus enforces coherence between *rendered* depth and normals, whereas $\mathcal{L}_{\text{orient}}$ provides direct supervision on the predicted Gaussian orientations, independent of the rasterizer.

In practice, naively applying \mathcal{L}_{RNC} in our generalizable splatting setup often causes the optimization of Gaussian means and orientations to converge to a near-planar local minimum (see Figure 12). Detaching the rendered depth from the computation graph alleviates this by treating the depth-derived normals as pseudo labels for Gaussian orientations, but this configuration still requires the alignment loss $\mathcal{L}_{\text{align}}$ to be effective. Table 12 compares models trained with $\mathcal{L}_{\text{align}} + \mathcal{L}_{\text{RNC}}$ against our full model using $\mathcal{L}_{\text{align}} + \mathcal{L}_{\text{orient}}$, showing that our orientation prior is more stable and yields better geometry. Unless otherwise stated, *all* 2DGS and 3DGS results reported in the main paper and supplementary use only $\mathcal{L}_{\text{align}}$ and $\mathcal{L}_{\text{orient}}$; \mathcal{L}_{RNC} is used solely as an ablation baseline in Table 12.

10. Depth Rendering for Gaussian Splatting

To evaluate geometry (depth and meshes), we must convert the Gaussian representation into a per-pixel depth map. Along each camera ray, multiple Gaussians may contribute, so there is no uniquely defined “depth.” In this work we considered two choices, both consistent with standard alpha compositing.

Recall that for a pixel (u, v) in view f , the rendered color is obtained by alpha-blending depth-sorted projected Gaussians \mathcal{G}'_k as

$$\hat{\mathbf{I}}_f(u, v) = \sum_{k=1}^K \mathbf{c}_k w_k(u, v), \quad (18)$$

$$w_k(u, v) = T_k(u, v) \alpha_k \mathcal{G}'_k(u, v), \quad (19)$$

$$T_k(u, v) = \prod_{i < k} (1 - \alpha_i \mathcal{G}'_i(u, v)), \quad (20)$$

where \mathbf{c}_k and α_k denote the color and opacity of Gaussian \mathcal{G}_k , and $\mathcal{G}'_k(u, v)$ is its 2D footprint in the image plane of \mathbf{I}_f .

For depth rendering, we reuse the same weights $w_k(u, v)$ but replace the color \mathbf{c}_k by the scalar depth $d_k(u, v)$ of Gaussian \mathcal{G}_k in the camera coordinate system. For brevity, we write $\mathbf{x} = (u, v)$ and index the Gaussians along the ray by i .

Accumulated depth. A common practice is to treat depth as an additional “channel” and apply the same alpha-

blending rule as for RGB. This yields an *accumulated depth*

$$D_{\text{acc}}(\mathbf{x}) = \sum_i w_i(\mathbf{x}) d_i(\mathbf{x}), \quad (21)$$

where $w_i(\mathbf{x})$ is defined as in (18). This definition aggregates contributions from all Gaussians along the ray and implicitly couples depth with the overall opacity.

Expected depth. Alternatively, we can interpret the weights $w_i(\mathbf{x})$ as defining a discrete distribution along the ray and compute the *expected depth*:

$$D_{\text{exp}}(\mathbf{x}) = \frac{\sum_i w_i(\mathbf{x}) d_i(\mathbf{x})}{\sum_i w_i(\mathbf{x})}, \quad (22)$$

Compared to D_{acc} , this normalizes out the accumulated opacity and is less sensitive to residual transmittance or brightness variations.

Choice of baseline depth renderer. We implemented both D_{acc} and D_{exp} and compared them quantitatively for our model. In contrast to existing generalizable Gaussian splatting works that effectively rely on accumulated depth, we found that the expected depth D_{exp} consistently yields lower depth errors and more stable TSDF fusion [8], resulting in higher-quality mesh reconstructions. In particular, Table 11 compares a re-trained NoPoSplat checkpoint (under our protocol) with its public checkpoint, and reports depth evaluation for our “no prior” baselines with both 2DGS and 3DGS representations.

Consequently, we adopt D_{exp} in (22) as our default depth rendering and use it for all “no prior” baselines. All proposed priors (alignment and orientation) are built on top of this expected-depth renderer and ablated accordingly.

11. Test-time Pose Refinement

For two-view reconstruction, many different 3D configurations can explain the same image pair, so even if a model produces a self-consistent scene, its recovered camera poses may not coincide exactly with the ground-truth poses in the evaluation datasets. Following the spirit of prior pose-free works, including [68], we therefore allow an optional test-time pose refinement step for fair comparison against pose-aware baselines.

Given an input pair, we first run the network once to predict the Gaussian splats from the source views. During evaluation, these Gaussian parameters are *frozen*, and we optimize the given camera pose by minimizing the same photometric objectives used at train time. Concretely, for a given view f with ground-truth image \mathbf{I}_f and rendered image $\hat{\mathbf{I}}_f(\mathbf{R}_f, \mathbf{T}_f)$, we solve a small gradient-based optimization problem

$$\min_{\mathbf{R}_f, \mathbf{T}_f} \mathcal{L}_{\text{synthesis}}(\mathbf{I}_f, \hat{\mathbf{I}}_f) + \lambda_a \mathcal{L}_{\text{align}} + \lambda_o \mathcal{L}_{\text{orient}},$$

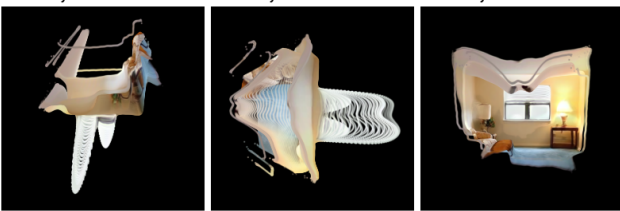
Table 12. **Ablation of Gaussian orientation losses.** We compare a model trained with $\mathcal{L}_{\text{align}} + \mathcal{L}_{\text{RNC}}$ against our full model trained with $\mathcal{L}_{\text{align}} + \mathcal{L}_{\text{orient}}$. (a) Pose evaluation with test-time refinement (same loss as training) on RE10K [75], ScanNet [9], and ACID [40]. (b) Novel-view depth estimation with pose refinement on ScanNet. (c) Novel-view synthesis on RE10K.

(a) Pose evaluation									
Method	RE10K			ScanNet-V1			ACID		
	5° ↑	10° ↑	20° ↑	5° ↑	10° ↑	20° ↑	5° ↑	10° ↑	20° ↑
Ours (2DGS+Align+RNC)	0.681	0.799	0.870	0.137	0.313	0.521	0.476	0.609	0.720
Ours (2DGS+Align+Orient)	0.686	0.802	0.875	0.153	0.334	0.541	0.478	0.609	0.723

(b) Depth evaluation									
Method	Rendered Depth (Novel Views)								
	Abs Rel↓	$\delta_1 < 1.10 \uparrow$	$\delta_1 < 1.25 \uparrow$						
Ours (2DGS+Align+RNC)	0.099		0.714		0.910				
Ours (2DGS+Align+Orient)	0.082		0.743		0.931				

(c) Novel-view synthesis												
Method	Small			Medium			Large			Average		
	PSNR↑	SSIM↑	LPIPS↓									
Ours (2DGS+Align+RNC)	21.344	0.736	0.236	23.423	0.786	0.185	25.432	0.825	0.141	23.501	0.785	0.185
Ours (2DGS+Align+Orient)	21.377	0.739	0.234	23.426	0.787	0.184	25.459	0.827	0.141	23.504	0.787	0.184

\mathcal{L}_{RNC} and $\mathcal{L}_{\text{align}}$



\mathcal{L}_{RNC} Only

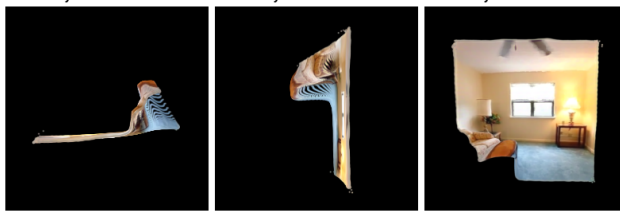


Figure 12. **Failure modes of rendered normal-depth consistency compared to our orientation loss.** We replace the proposed orientation prior $\mathcal{L}_{\text{orient}}$ with the rendered normal-depth consistency loss \mathcal{L}_{RNC} [26] and visualize the learned scene during training on RE10K [75], by projecting the reconstructed 3D Gaussians onto three axis-aligned planes. Using \mathcal{L}_{RNC} without the alignment loss $\mathcal{L}_{\text{align}}$ yields severely degenerate reconstructions. Adding $\mathcal{L}_{\text{align}}$ recovers some structure but remains clearly inferior to the results obtained with $\mathcal{L}_{\text{align}} + \mathcal{L}_{\text{orient}}$ reported in the main paper.

where only the pose parameters ($\mathbf{R}_f, \mathbf{T}_f$) are updated and all Gaussian parameters remain fixed. For each model variant, we include exactly the same loss terms as used during training (e.g., $\mathcal{L}_{\text{align}}$ and/or $\mathcal{L}_{\text{orient}}$), so that the pose refinement is consistent with the learned priors.

We use this test-time pose refinement in two contexts: (i) for pose evaluation, where the refined pose is compared against ground truth using rotation and translation error metrics; and (ii) for depth evaluation, where we render depth maps from the refined camera pose to disentangle errors due to misaligned camera poses from errors in the underlying scene structure. All relevant pose and depth evaluations results are reported both *with* and *without* this pose refinement scheme, and whenever refinement is used it is explicitly stated in the corresponding table or figure caption.

12. Mesh Reconstruction and Evaluation

Predicted mesh reconstruction. For each ScanNet [9] test scene, we first predict a Gaussian-splatting representation from two source views using our model (either DUS3R- or VGGT-based). The predicted Gaussians are then used to render depth maps from a virtual camera trajectory interpolated between the two source poses. Concretely, we sample a fixed number of intermediate viewpoints (20 in our implementation) by smoothly interpolating extrinsics between the two input cameras, and use our expected-depth renderer (Sec. Section 10) to obtain per-view rendered depth maps along this path. These depth maps, together with the corresponding camera intrinsics and extrinsics, are fused into a volumetric TSDF using TSDF-Fusion [8]. We use a scene-adaptive voxel size (proportional to the scene radius) and a standard truncation distance (a small multiple of the voxel

size), and extract a watertight surface mesh via Marching Cubes. Finally, we keep the largest connected component and remove small isolated clusters and degenerate faces, yielding the predicted mesh for that scene.

Ground-truth meshes and visibility cropping. ScanNet provides a metric-scale mesh for each scene. We rigidly transform this mesh into the coordinate frame where the first source camera is placed at the origin.

To avoid penalizing geometry that is never observed in the source views, we crop the ground-truth mesh to the region seen by the cameras. Specifically, we construct the union of viewing frusta of the source frames and intersect the mesh with this union. The resulting cropped mesh is used as the ground-truth surface for evaluation.

Global Sim(3) alignment. Because our pose-free model is trained without metric depth or absolute pose supervision, the recovered scene geometry and cameras are only defined up to a global Sim(3) transform (rotation, translation, and uniform scale). Before computing metrics, we therefore align each predicted mesh to its ground-truth counterpart using a single global Sim(3) transformation. Concretely, we sample points from the surfaces of both the predicted mesh and the cropped ground-truth mesh, and run a point-to-point ICP procedure with scaling to estimate the best-fitting similarity transform between them. This transform is then applied to the predicted mesh, and all reconstruction metrics are computed in the resulting aligned, metric coordinate frame.

Evaluation metrics. Let $P = \{\mathbf{p}_i\}_{i=1}^{N_p}$ and $G = \{\mathbf{g}_j\}_{j=1}^{N_g}$ be point sets sampled uniformly from the aligned predicted mesh and the cropped ground-truth mesh, respectively. For each point $\mathbf{p}_i \in P$, we compute the distance to its nearest neighbor in G ,

$$d_{\text{pred} \rightarrow \text{gt}}(\mathbf{p}_i) = \min_{\mathbf{g} \in G} \|\mathbf{p}_i - \mathbf{g}\|_2,$$

and similarly for each $\mathbf{g}_j \in G$ we compute

$$d_{\text{gt} \rightarrow \text{pred}}(\mathbf{g}_j) = \min_{\mathbf{p} \in P} \|\mathbf{g}_j - \mathbf{p}\|_2.$$

We report three standard reconstruction metrics [23, 42]:

- **Accuracy** (lower is better):

$$\text{Acc} = \frac{1}{N_p} \sum_{i=1}^{N_p} d_{\text{pred} \rightarrow \text{gt}}(\mathbf{p}_i),$$

measuring how close the predicted surface lies to the nearest ground-truth surface.

- **Completeness** (lower is better):

$$\text{Comp} = \frac{1}{N_g} \sum_{j=1}^{N_g} d_{\text{gt} \rightarrow \text{pred}}(\mathbf{g}_j),$$

measuring how well the predicted mesh covers the ground-truth surface.

- **Chamfer distance** (lower is better):

$$\text{CD} = \frac{1}{2} (\text{Acc} + \text{Comp}),$$

the symmetric Chamfer distance between P and G .

Per-scene scores are averaged over all ScanNet test scenes where both predicted and ground-truth meshes are non-empty after reconstruction and cropping. These aggregated metrics are reported in Table 5.

References

[1] Jia-Wang Bian, Huangying Zhan, Naiyan Wang, Tat-Jun Chin, Chunhua Shen, and Ian Reid. Auto-rectify network for unsupervised indoor depth estimation. *IEEE transactions on pattern analysis and machine intelligence*, 44(12):9802–9813, 2021. 2, 4

[2] Jia-Ren Chang and Yong-Sheng Chen. Pyramid stereo matching network. In *CVPR*, 2018. 3

[3] David Charatan, Sizhe Lester Li, Andrea Tagliasacchi, and Vincent Sitzmann. pixelsplat: 3d gaussian splats from image pairs for scalable generalizable 3d reconstruction. In *CVPR*, 2024. 1, 2, 4, 6, 8, 5

[4] Danpeng Chen, Hai Li, Weicai Ye, Yifan Wang, Weijian Xie, Shangjin Zhai, Nan Wang, Haomin Liu, Hujun Bao, and Guofeng Zhang. Pgss: Planar-based gaussian splatting for efficient and high-fidelity surface reconstruction. *TVCG*, 2024. 2

[5] Yuedong Chen, Haofei Xu, Chuanxia Zheng, Bohan Zhuang, Marc Pollefeys, Andreas Geiger, Tat-Jen Cham, and Jianfei Cai. Mvsplat: Efficient 3d gaussian splatting from sparse multi-view images. In *ECCV*, 2024. 1, 2, 3, 4, 6, 8, 5

[6] Shin-Fang Chng, Ravi Garg, Hemanth Saratchandran, and Simon Lucey. Invertible neural warp for nerf. In *ECCV*, 2024. 3

[7] Jaeyoung Chung, Jeongtaek Oh, and Kyoung Mu Lee. Depth-regularized optimization for 3d gaussian splatting in few-shot images. In *CVPR*, 2024. 2, 3

[8] Brian Curless and Marc Levoy. A volumetric method for building complex models from range images. In *Proceedings of the 23rd annual conference on Computer graphics and interactive techniques*, pages 303–312, 1996. 9, 5, 12, 13

[9] Angela Dai, Angel X Chang, Manolis Savva, Maciej Halber, Thomas Funkhouser, and Matthias Nießner. Scannet: Richly-annotated 3d reconstructions of indoor scenes. In *CVPR*, 2017. 2, 6, 7, 8, 9, 1, 4, 5, 10, 11, 13

[10] Yilun Du, Cameron Smith, Ayush Tewari, and Vincent Sitzmann. Learning to render novel views from wide-baseline stereo pairs. In *CVPR*, 2023. 5

[11] Johan Edstedt, Qiyu Sun, Georg Bökman, Mårten Wadenbäck, and Michael Felsberg. Roma: Robust dense feature matching. In *CVPR*, 2024. 2, 6, 7

[12] David Eigen and Rob Fergus. Predicting depth, surface normals and semantic labels with a common multi-scale convolutional architecture. In *Proceedings of the IEEE international conference on computer vision*, pages 2650–2658, 2015. 5

[13] David Eigen, Christian Puhrsch, and Rob Fergus. Depth map prediction from a single image using a multi-scale deep network. In *NeurIPS*, 2014. 3

[14] Huan Fu, Mingming Gong, Chaohui Wang, Kayhan Batmanghelich, and Dacheng Tao. Deep ordinal regression network for monocular depth estimation. In *CVPR*, 2018. 3

[15] Yang Fu, Sifei Liu, Amey Kulkarni, Jan Kautz, Alexei A Efros, and Xiaolong Wang. Colmap-free 3d gaussian splatting. In *CVPR*, 2024. 4

[16] Ravi Garg, Vijay Kumar Bg, Gustavo Carneiro, and Ian Reid. Unsupervised cnn for single view depth estimation: Geometry to the rescue. In *ECCV*, 2016. 4

[17] Ravi Garg, Shin-Fang Chng, and Simon Lucey. Direct alignment for robust nerf learning. In *ACCV*, 2024. 3

[18] Clément Godard, Oisin Mac Aodha, and Gabriel J Brostow. Unsupervised monocular depth estimation with left-right consistency. In *CVPR*, 2017. 4

[19] Clement Godard, Oisin Mac Aodha, Michael Firman, and Gabriel J. Brostow. Digging into self-supervised monocular depth estimation. In *ICCV*, 2019. 4

[20] Clément Godard, Oisin Mac Aodha, Michael Firman, and Gabriel J Brostow. Digging into self-supervised monocular depth estimation. In *Proceedings of the IEEE/CVF international conference on computer vision*, pages 3828–3838, 2019. 2, 4

[21] Xiaodong Gu, Zhiwen Fan, Siyu Zhu, Zuozhuo Dai, Feitong Tan, and Ping Tan. Cascade cost volume for high-resolution multi-view stereo and stereo matching. In *CVPR*, 2020. 3

[22] Antoine Guédon and Vincent Lepetit. Sugar: Surface-aligned gaussian splatting for efficient 3d mesh reconstruction and high-quality mesh rendering. *CVPR*, 2024. 3

[23] Haoyu Guo, Sida Peng, Haotong Lin, Qianqian Wang, Guofeng Zhang, Hujun Bao, and Xiaowei Zhou. Neural 3d scene reconstruction with the manhattan-world assumption. In *Proceedings of the IEEE/CVF conference on computer vision and pattern recognition*, pages 5511–5520, 2022. 9, 14

[24] Liang Han, Junsheng Zhou, Yu-Shen Liu, and Zhizhong Han. Binocular-guided 3d gaussian splatting with view consistency for sparse view synthesis. *NeurIPS*, 2024. 3

[25] Sunghwan Hong, Jaewoo Jung, Heeseong Shin, Jiaolong Yang, Seungryong Kim, and Chong Luo. Unifying correspondence pose and nerf for generalized pose-free novel view synthesis. In *CVPR*, 2024. 6, 7, 5

[26] Binbin Huang, Zehao Yu, Anpei Chen, Andreas Geiger, and Shenghua Gao. 2d gaussian splatting for geometrically accurate radiance fields. In *ACM SIGGRAPH 2024*, 2024. 2, 3, 4, 5, 10, 11, 13

[27] Jia-Bin Huang, Iain Matthews, and Wolf Kienzle. Deepmvs: Learning multi-view stereopsis. In *CVPR*, 2018. 3

[28] Lihang Jiang, Yucheng Mao, Lining Xu, Tao Lu, Kerui Ren, Yichen Jin, Xudong Xu, Mulin Yu, Jiangmiao Pang, Feng Zhao, et al. Anysplat: Feed-forward 3d gaussian splatting from unconstrained views. *arXiv preprint arXiv:2505.23716*, 2025. 1, 4, 9

[29] Seunghyun Kang, Hyunwoo Lee, and Hyeongju Chae. Self-splat: Pose-free and 3d-prior-free generalizable 3d gaussian splatting. *CVPR*, 2025. 1, 4, 7, 8, 5

[30] Nikhil Keetha, Jay Karhade, Krishna Murthy Jatavallabhula, Gengshan Yang, Sebastian Scherer, Deva Ramanan, and Jonathon Luiten. Splatam: Splat, track & map 3d gaussians for dense rgb-d slam. In *CVPR*, 2024. 3

[31] Bernhard Kerbl, Georgios Kopanas, Thomas Leimkühler, and George Drettakis. 3d gaussian splatting for real-time radiance field rendering. *ACM TOG*, 2023. 1, 2, 3, 10

[32] Arno Knapitsch, Jaesik Park, Qian-Yi Zhou, and Vladlen Koltun. Tanks and temples: Benchmarking large-scale scene reconstruction. *ACM TOG*, 2017. 4

[33] Iro Laina, Christian Rupprecht, Vasileios Belagiannis, Federico Tombari, and Nassir Navab. Deeper depth prediction with fully convolutional residual networks. In *3DV*, 2016. 3

[34] Jin Han Lee, Youngbok Bae, and In So Kweon Han. Bts: Depth estimation via local planar guidance. *arXiv preprint arXiv:1907.10326*, 2019. 3

[35] Vincent Leroy, Yohann Cabon, and Jérôme Revaud. Grounding image matching in 3d with mast3r. *arXiv preprint arXiv:2406.09756*, 2024. 1, 2, 3, 4, 6, 7, 10

[36] Jiahe Li, Jiawei Zhang, Xiao Bai, Jin Zheng, Xin Ning, Jun Zhou, and Lin Gu. Dngaussian: Optimizing sparse-view 3d gaussian radiance fields with global-local depth normalization. In *CVPR*, 2024. 3

[37] Mingrui Li, Shuhong Liu, Heng Zhou, Guohao Zhu, Na Cheng, Tianchen Deng, and Hongyu Wang. Sgs-slam: Semantic gaussian splatting for neural dense slam. In *ECCV*, 2024. 3

[38] Zhengqi Li and Noah Snavely. Megadepth: Learning single-view depth prediction from internet photos. In *CVPR*, 2018. 6

[39] Zhan Li, Zhang Chen, Zhong Li, and Yi Xu. Spacetime gaussian feature splatting for real-time dynamic view synthesis. In *CVPR*, 2024. 3

[40] Andrew Liu, Richard Tucker, Varun Jampani, Ameesh Makadia, Noah Snavely, and Angjoo Kanazawa. Infinite nature: Perpetual view generation of natural scenes from a single image. In *ICCV*, 2021. 6, 7, 4, 5, 11, 13

[41] Hidenobu Matsuki, Riku Murai, Paul HJ Kelly, and Andrew J Davison. Gaussian splatting slam. In *CVPR*, 2024. 3, 6

[42] Lars Mescheder, Michael Oechsle, Michael Niemeyer, Sebastian Nowozin, and Andreas Geiger. Occupancy networks: Learning 3d reconstruction in function space. In *Proceedings of the IEEE/CVF conference on computer vision and pattern recognition*, pages 4460–4470, 2019. 14

[43] Zhiyuan Min, Yawei Luo, Jianwen Sun, and Yi Yang. Epipolar-free 3d gaussian splatting for generalizable novel view synthesis. *NeurIPS*, 2024. 4

[44] OpenAI. Creating video from text, 2024. 1

[45] René Ranftl, Alexey Bochkovskiy, and Vladlen Koltun. Vision transformers for dense prediction. In *ICCV*, 2021. 3

[46] Johannes L Schonberger and Jan-Michael Frahm. Structure-from-motion revisited. In *CVPR*, 2016. 6

[47] Nathan Silberman, Derek Hoiem, Pushmeet Kohli, and Rob Fergus. Indoor segmentation and support inference from rgbd images. In *Computer Vision–ECCV 2012: 12th European Conference on Computer Vision, Florence, Italy, October 7–13, 2012, Proceedings, Part V 12*, pages 746–760. Springer, 2012. 2, 4

[48] Brandon Smart, Chuanxia Zheng, Iro Laina, and Victor Adrian Prisacariu. Splatt3r: Zero-shot gaussian splatting from uncalibrated image pairs. *arXiv preprint arXiv:2408.13912*, 2024. 1, 4, 7, 8, 3, 5

[49] Libo Sun, Jia-Wang Bian, Huangying Zhan, Wei Yin, Ian Reid, and Chunhua Shen. Sc-depthv3: Robust self-supervised monocular depth estimation for dynamic scenes. *IEEE transactions on pattern analysis and machine intelligence*, 46(1):497–508, 2023. 2, 4

[50] Pei Sun, Henrik Kretzschmar, Xerxes Dotiwalla, Aurelien Chouard, Vijaysai Patnaik, Paul Tsui, James Guo, Yin Zhou, Yuning Chai, Benjamin Caine, et al. Scalability in perception for autonomous driving: Waymo open dataset. In *CVPR*, 2020. 6

[51] Stanislaw Szymanowicz, Eldar Insafutdinov, Chuanxia Zheng, Dylan Campbell, Joao F Henriques, Christian Rupprecht, and Andrea Vedaldi. Flash3d: Feed-forward generalisable 3d scene reconstruction from a single image. In *2025 International Conference on 3D Vision (3DV)*, pages 670–681. IEEE, 2025. 1

[52] Shengji Tang, Weicai Ye, Peng Ye, Weihao Lin, Yang Zhou, Tao Chen, and Wanli Ouyang. Hisplat: Hierarchical 3d gaussian splatting for generalizable sparse-view reconstruction. *ICLR*, 2025. 4

[53] Benjamin Ummenhofer, Hao Zhou, Jonas Uhrig, Nikolaus Mayer, Eddy Ilg, Alexey Dosovitskiy, and Thomas Brox. Demon: Depth and motion network for learning monocular stereo. In *CVPR*, 2017. 3

[54] Ziyu Wan, Hao Gao, Rui Xiong, and Fang Du. S2gaussian: Sparse-view super-resolution 3d gaussian splatting. In *CVPR*, 2025. 3

[55] Fangjinhua Wang, Silvano Galliani, Christoph Vogel, Pablo Speciale, and Marc Pollefeys. Patchmatchnet: Learned multi-view patchmatch stereo. In *CVPR*, 2021. 3

[56] Jianyuan Wang, Minghao Chen, Nikita Karaev, Andrea Vedaldi, Christian Rupprecht, and David Novotny. Vggt: Visual geometry grounded transformer. In *Proceedings of the IEEE/CVF Conference on Computer Vision and Pattern Recognition*, 2025. 1, 2, 3, 8, 9, 5, 10

[57] Qianqian Wang, Yifei Zhang, Aleksander Holynski, Alexei A. Efros, and Angjoo Kanazawa. Continuous 3d perception model with persistent state. In *CVPR*, 2025. 3

[58] Shuzhe Wang, Vincent Leroy, Yohann Cabon, Boris Chidlovskii, and Jerome Revaud. Dust3r: Geometric 3d vision made easy. In *CVPR*, 2024. 1, 2, 3, 6, 7, 8, 9, 4, 5

[59] Yunsong Wang, Tianxin Huang, Hanlin Chen, and Gim Hee Lee. Freesplat: Generalizable 3d gaussian splatting towards free view synthesis of indoor scenes. *NeurIPS*, 2024. 1, 4, 8, 5, 10

[60] Guanjun Wu, Taoran Yi, Jiemin Fang, Lingxi Xie, Xiaopeng Zhang, Wei Wei, Wenyu Liu, Qi Tian, and Xinggang Wang. 4d gaussian splatting for real-time dynamic scene rendering. In *CVPR*, 2024. 3

[61] Haolin Xiong, Sairisheek Muttukuru, Rishi Upadhyay, Pradyumna Chari, and Achuta Kadambi. Sparsegs: Real-time 360° sparse view synthesis using gaussian splatting. In *3DV*, 2025. 3

[62] Haofei Xu, Jing Zhang, Jianfei Cai, Hamid Rezatofighi, Fisher Yu, Dacheng Tao, and Andreas Geiger. Unifying flow, stereo and depth estimation. *IEEE Transactions on Pattern Analysis and Machine Intelligence*, 45(11):13941–13958, 2023. 1, 2, 4

[63] Haofei Xu, Songyou Peng, Fangjinhua Wang, Hermann Blum, Daniel Barath, Andreas Geiger, and Marc Pollefeys. Depthsplat: Connecting gaussian splatting and depth. In *CVPR*, 2025. 1, 4, 8, 2, 5

[64] Lihe Yang, Bingyi Kang, Zilong Huang, Zhen Zhao, Xiaogang Xu, Jiashi Feng, and Hengshuang Zhao. Depth anything v2. *arXiv:2406.09414*, 2024. 2

[65] Ziyi Yang, Xinyu Gao, Wen Zhou, Shaohui Jiao, Yuqing Zhang, and Xiaogang Jin. Deformable 3d gaussians for high-fidelity monocular dynamic scene reconstruction. In *CVPR*, 2024. 3

[66] Zeyu Yang, Hongye Yang, Zijie Pan, and Li Zhang. Real-time photorealistic dynamic scene representation and rendering with 4d gaussian splatting. In *ICLR*, 2024. 3

[67] Yao Yao, Zixin Luo, Shiwei Li, Tian Fang, and Long Quan. Mvsnet: Depth inference for unstructured multi-view stereo. In *ECCV*, 2018. 3

[68] Botao Ye, Sifei Liu, Haofei Xu, Li Xuetong, Marc Pollefeys, Ming-Hsuan Yang, and Peng Songyou. No pose, no problem: Surprisingly simple 3d gaussian splats from sparse unposed images. In *ICLR*, 2025. 1, 2, 3, 4, 6, 7, 8, 5, 10, 12

[69] Chandan Yeshwanth, Yueh-Cheng Liu, Matthias Nießner, and Angela Dai. Scannet++: A high-fidelity dataset of 3d indoor scenes. In *ICCV*, 2023. 6

[70] Alex Yu, Vickie Ye, Matthew Tancik, and Angjoo Kanazawa. pixelnerf: Neural radiance fields from one or few images. In *CVPR*, 2021. 5

[71] Huangying Zhan, Ravi Garg, Chamara Saroj Weerasekera, Kejie Li, Harsh Agarwal, and Ian Reid. Unsupervised learning of monocular depth estimation and visual odometry with deep feature reconstruction. In *CVPR*, 2018. 4

[72] Shunyuan Zheng, Boyao Zhou, Ruizhi Shao, Boning Liu, Shengping Zhang, Liqiang Nie, and Yebin Liu. Gps-gaussian: Generalizable pixel-wise 3d gaussian splatting for real-time human novel view synthesis. In *CVPR*, 2024. 1, 4

[73] Qian-Yi Zhou, Jaesik Park, and Vladlen Koltun. Open3d: A modern library for 3d data processing. *arXiv preprint arXiv:1801.09847*, 2018. 2

[74] Tinghui Zhou, Matthew Brown, Noah Snavely, and David G Lowe. Unsupervised learning of depth and ego-motion from video. In *CVPR*, 2017. 4

[75] Tinghui Zhou, Richard Tucker, John Flynn, Graham Fyffe, and Noah Snavely. Stereo magnification: learning view synthesis using multiplane images. *ACM TOG*, 2018. 1, 6, 7, 3, 4, 5, 8, 10, 11, 13

[76] Zihan Zhu, Songyou Peng, Viktor Larsson, Weiwei Xu, Hujun Bao, Zhaopeng Cui, Martin R Oswald, and Marc Pollefeys. Nice-slam: Neural implicit scalable encoding for slam. In *CVPR*, 2022. 4, 9

[77] Zehao Zhu, Zhiwen Fan, Yifan Jiang, and Zhangyang Wang. Fsgs: Real-time few-shot view synthesis using gaussian splatting. In *ECCV*, 2024. 2, 3

[78] Zihan Zhu, Songyou Peng, Viktor Larsson, Zhaopeng Cui, Martin R Oswald, Andreas Geiger, and Marc Pollefeys. Nicerslam: Neural implicit scene encoding for rgb slam. In *3DV*, 2024. 4